6-4-2019

Distribution and Origin of Carbide in Ordinary Chondrites

Karla Rae Farley
Portland State University

Distribution and Origin of Carbide in Ordinary Chondrites

by

Karla Rae Farley

A thesis submitted in partial fulfillment of the
requirements for the degree of

Master of Science
in
Geology

Thesis Committee:
Alexander Ruzicka, Chair
Melinda Hutson
Richard Hugo

Portland State University
2019

Abstract

To understand the occurrence and distribution of carbide minerals in ordinary chondrites, thirty meteorites were examined, twenty-eight ordinary chondrites and two iron meteorites. The occurrence of carbide, textures, and chemical compositions were examined in the 7 carbide-bearing meteorites. Two formation methods for carbide have been presented in previous research. These are aqueous alteration and shock heating, and they are examined for validity in this thesis. Additionally, one other formation method for carbide formation through impact and brecciation is put forth and examined. Textural differences between the carbide-magnetite assemblages (CMAs) observed by Krot et al., (1997) and those seen in this study are compared regarding possible evidence for aqueous alteration. Different carbide minerals (haxonite and cohenite) were distinguished using a correction method on linescan data obtained through a scanning election microscope. Cooling rates, formation temperatures, and closure temperatures from carbide associated taenites closely match that of petrographic type 3 material from ordinary chondrites. Carbide is not found in shock melt, and shock blackened areas are less likely to contain carbide. It is unlikely that the heat source that formed carbides exceeded that of petrographic type 3 as too much heat would equilibrate the type 3 material as well as carbide minerals or prevent them from forming.

Acknowledgements

I would like to thank Kristy Schepker for her previous work on digitizing the FeNi phase diagram of Reisener and Goldstein (2003a, b).

Table of Contents

List of Tables

List of Figures

Introduction

Chondrites are stony meteorites that were not melted overall, but which experienced thermal metamorphism to various extents. Ordinary (O) chondrites are the most numerous kinds of chondrite, and can be subdivided into H, L, and LL types based on metal content and chondrule mean diameter (Krot et al., 2005, Brearley et al, 1998). Thermal metamorphism can be designated by petrographic types that range from 3 to 6 for ordinary chondrites, with type 3 the least metamorphosed and type 6 the most (Krot et al., 2005, Weisberg et al., 2006). Type 3 chondrites can be subdivided into subtypes ranging from 3.0 (least heated) to 3.9 (more heated) (Grossman and Brearley, 2005, Huss et al., 2006).

Besides thermal metamorphism, ordinary chondrites can experience aqueous alteration, although this has primarily been described in ordinary chondrites of low subtype (3.0-3.2). These include Semarkona, Bishunpur, and Chainpur. Aqueous alteration is seen most easily through the formation of secondary mineral phases (Brearley, 2006). Additionally, the widespread presence of bleached chondrules in type 3 chondrites indicates that aqueous alteration may have been more pervasive as these appear to have formed by aqueous alteration. Bleached chondrules been found in all three ordinary chondrite groups as well as in petrographic types 3-6, although less frequent in the higher types and H chondrites (Grossman et al., 2000).

Shock metamorphism by hypervelocity impacts occurs in ordinary chondrites (Stöffler et al., 1988, 1991). Shock metamorphism can be designated petrographically by

stages based on the characteristics of olivine observed with optical microscopy reflecting the plastic deformation of the mineral. There are six stages which range from S1 (lightly shocked) to S6 (shock recrystallized), with even stronger shocks resulting in impact melt rocks (Stöffler et al., 1991). In addition to plastic deformation and melting, impact processes also produced breccias of different kinds. These include genomict breccias that are composed of fragments of different metamorphic grades (petrographic types), regolith breccias that show indicators of surface exposure on an asteroidal parent body, impact-melt breccias that contain unmelted clasts set amidst impact melt, and fragmental breccias containing clasts of impact melt (Bischoff et al., 2006).

Carbide minerals are known to occur as a common byproduct of steel production and are relatively common in iron meteorites (e.g., Buchwald, 1975) but have not been recognized to be widely present in ordinary chondrites. However, recently these minerals have been detected in several ordinary chondrites (Likkel et al., 2013, Schepker 2014, Hutson et al., 2016) and are the focus of this study. At least two types of carbides have been identified in ordinary chondrites, cohenite [$(Fe, Ni)_3C$] and haxonite [$(Fe, Ni)_{23}C_6$] (Krot et al., 1997, Hutson et al., 2016). They can be identified with reflected light microscopy, as grains that appear light pink/tan in color, usually partly within and at the edges of metal grains Figure 1.

The origins of such carbide minerals are not known. However, one suggestion is that they were produced by aqueous alteration of FeNi-metal on the parent body in a process that also created magnetite (Krot et al., 1997). This hypothesis would predict that carbides should be associated with evidence for aqueous alteration, probably in weakly

metamorphosed (type 3) ordinary chondrites in which aqueous alteration effects are mainly reported (Brearley, 2006). Another possibility is that carbides were produced by shock-heating of carbon-bearing materials and reaction with metal (Hauver and Ruzicka, 2011; Likkel et al., 2013; Schepker, 2014, Hutson et al., 2016). This hypothesis would predict that carbides should be associated with shock effects, such as evidence for shock melts or other evidence for increased shock as manifested by a higher shock stage.

This thesis will test these two hypotheses and evaluate the origin of carbide in ordinary chondrites, through examination of a variety of ordinary chondrites of different shock stages, metamorphic grades (petrographic types), and breccia types. Optical Microscopy (OM) and Scanning Electron Microscope (SEM) data were used to obtain petrographic and chemical data for carbides and associated metal phases. These data were used to evaluate the conditions on which carbide formed, and the nature of processes occurring on the (asteroidal) parent bodies.

Background

The first accounts of carbides in ordinary chondrites were in Semarkona (a type LL 3.0 chondrite), ALHA 77278 (LL 3.7), and Ngawi (LL 3.6) (Taylor et al., 1981). Fredriksson et al. (1989) found carbide assemblages in Study Butte (H3-6). ALHA 79003 (LL3.4), Khohar (L 3.6), and Piancaldoli (LL 3.4) contain carbide in the form of haxonite (Scott et al., 1982). And recently, carbides have also been described by Grokhovsky et al. (2015) in Chelyabinsk and by Harries and Langenhorst (2014) from the asteroid 25143 Itokawa.

Krot et al. (1997) did an in-depth analysis of 117 type 3 ordinary chondrites to find and study carbides. Krot et al. determined that carbides occurred in assemblages with magnetite. These assemblages were called CMAs for carbide-magnetite assemblages. The CMAs were found in matrix, chondrules, and chondrule rims of type 3 H, L, and LL ordinary chondrites. A typical CMA is layered, with a crude outer layer of magnetite surrounding carbide (cohenite or haxonite) and an FeNi-metal core (Krot et al., 1997). Krot et al suggested a formation that involved metal-troilite nodules that underwent hydrothermal alteration by a C-O-H-rich fluid. The iron-nickel metal then experienced carbidization by possibly a CO gas. This reaction could have proceeded as follows (Krot et al. 1997):

$$15\ Fe(s) + 4\ CO\ (g) = 4\ Fe_3C(s) + Fe_3O_4(s)\ [1]$$

or

$$3\ Fe(s) + 2\ CO(g) = Fe_3C(s) + CO_2(g)\ [2]$$

with reaction [2] followed by oxidation by H_2O, possibly by the following reaction:

$$3\ Fe(s) + 4H_2O(g) = Fe_3O_4(s) + 4H_2(g) \qquad [3]$$

Reactions [1]-[3] all involve reaction of metal with a gas and are thermodynamically favorable at low temperatures conditions on asteroidal parent bodies. Temperatures would need to be greater than 400 K to produce the necessary gases and carbide could form at temperatures less than 700 K with the most favorable reaction ([1]) that additionally, produced magnetite (Krot et al., 1997).

In a recent study by Schepker (2014), carbide grains were found in two chondrites, NWA 5964 and NWA 6580, which displayed no evidence for hydrothermal alteration or magnetite. Schepker (2014) found that the carbide grains are present in L chondrite melt breccias, close to but not within shock-melted regions. Carbides were not found in other meteorites, including a strongly shocked but largely unmelted S6 chondrite NWA 4860 nor in two L melt rocks NWA 6454 and NWA 6579 (Schepker 2014). Additional work by Likkel et al (2013) on NWA 5964 and Buck Mountain Wash supports formation by shock-induced contact metamorphism. These authors, along with Hutson et al (2016) suggest carbide formation through shock reheating, which caused the breakdown of type 3 material and the reincorporation of carbon into metal phases to form carbide.

Analytical Methods and Samples

Optical Microscopy

Optical Microscopy (OM) on thin sections was performed using a DM2500 Leica petrographic microscope with a digital camera and LAS software. Observations were made in plane polarized light, cross-polarized light, and reflected light imaging. Reflected light imaging was the primary method used to find and identify carbides in meteorite samples. Reflected light allowed details in the metal grains to be observed and the carbides differentiated from their surroundings. Maps were created to track carbide-bearing grains by inverting the reflected light mosaic using Adobe Photoshop and then marking the non-carbide bearing metals with purple and the carbide bearing metal grains in red.

Several features were used to identify carbides, color being one of the primary ways this was accomplished at high magnifications (50x objective) To optimize the likelihood of being able to visually identify the carbides, reflected light filters were adjusted to differentiate between kamacite, taenite, and troilite as much as possible. Saturation, brightness, and contrast were adjusted with LAS software until kamacite was a blue-white, taenite was a cream white, and troilite was an orange-brown. Carbide would then be salmon pink in coloration, as seen in Figure 1. However, it was not possible to optically distinguish between haxonite and cohenite. Additionally, this rendered magnetite as a grey/brown color while other oxides and weathers by-products were various shades of brighter grey and the silicates were dark grey, also seen in Figure 1.

Relief was another feature that was paired with color to identify carbides. Carbides would seemingly sit higher than the surrounding metal and that difference in relief can make them easier to see. Fractures are also often associated with carbide, with one or more bisecting fractures often crossing a carbide grain but not into surrounding metal, or fractures occurring adjacent to grain boundaries (Figure 1).

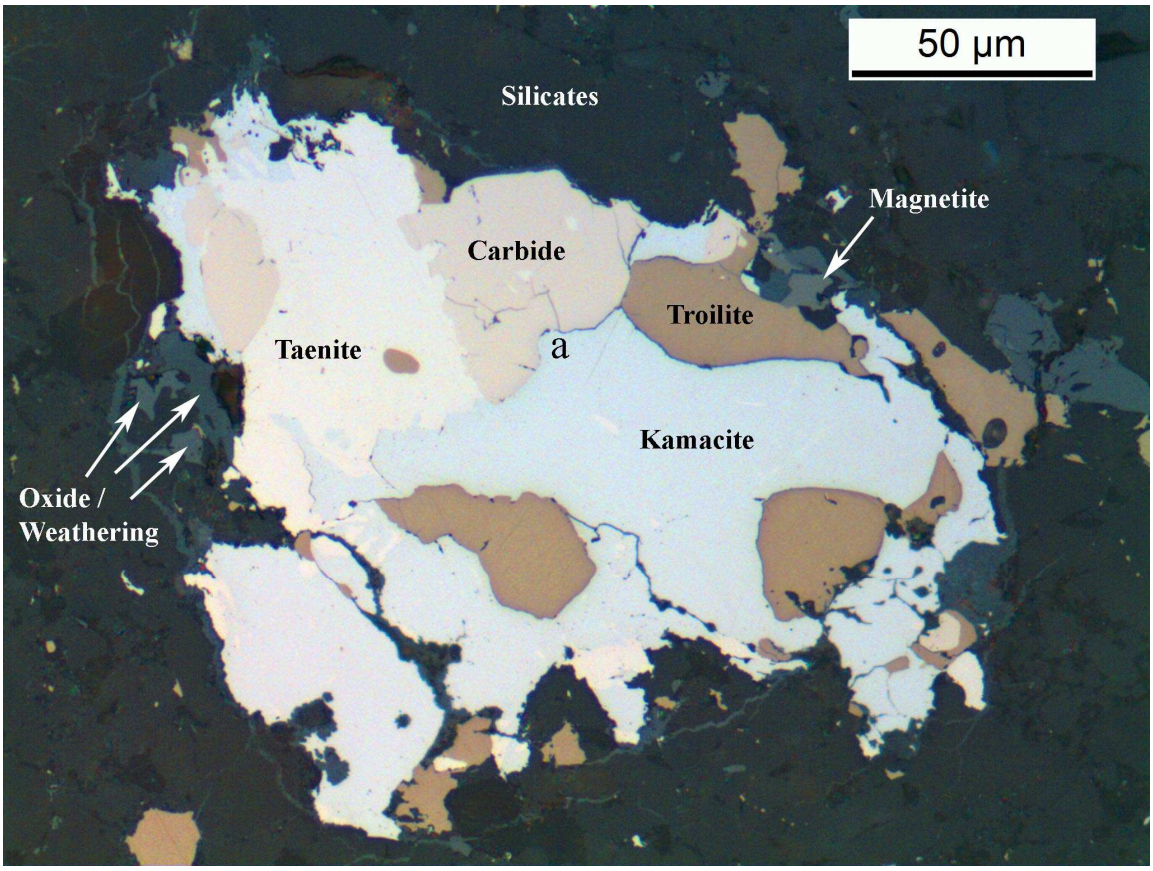

Figure 1. Illustrates the colors generally attributed to kamacite, taenite, troilite, carbide, magnetite, oxides, silicates, and weathering products in reflective light imaging. Fractures outline grains, as seen at "a" above. The picture above was given the designation 0157-2-C-440 from NWA 10518 (thin section CML 0157-2). Reflected light, image color enhanced.

To enhance visibility, images were color enhanced using Adobe Photoshop to increase the contrast and brightness. The curves feature was also used to fine tune the image.

SEM Analysis

Following carbon coating to typically ≤10 nm thickness, carbides and associated metal were analyzed using a Zeiss Sigma Field Emission-Variable Pressure (FE-VP) SEM with an attached high-efficiency XMax50 silicon-drift energy dispersive spectrometer (EDS) and Oxford Instruments AZtec 3.1-3.3 software, located in the Center for Electron Microscopy and Nanomaterials (CEMN) at Portland State University (PSU). The accelerating voltage for the SEM was set to 15 keV, and beam currents were 5-10 nA. Backscattered electron (BSE) imaging and EDS data were obtained. EDS data were obtained in the form of points with 45 seconds acquisition time, and linescan data for variable times (typically for 20-37 passes over several minutes acquisition time) to optimize the signal-to-noise in C and Ni count rates.

Quantitative phase chemical data were obtained by converting count rate data to concentrations using energy and beam calibration on a pure Cu standard and factory quantitative standardizations for elements of interest (Fe, Ni, C, S). In addition, a special procedure was used to correct C concentrations for the effect of carbon coat. This correction procedure was performed for linescans that included analysis of both carbide and adjacent metal grains. In these traverses, apparent C contents in metal grains (usually kamacite, which has typically lower C contents than taenite) were assumed to reflect entirely C coat, so that the actual C content of kamacite was zero. The average C content

in kamacite was averaged across that phase and this number (the assumed value of the C coat) was subtracted from the C contents for the carbide and metal phases in each linescan. This adjusted C content was the corrected apparent C content. The average Fe, Ni, and C contents were calculated for each phase and normalized to 100% after the correction.

Some linescans across taenite grains were obtained for the purpose of obtaining metallographic cooling rates. These were collected much the same way as those for carbides except that the linescans were aimed across the center of the taenite grain to obtain the best nickel zoning profile.

Cooling Rate Measurements

Cooling rate measurements were determined by taking the taenite linescans mentioned above and measuring the radius of the taenite grain and the nickel content at the center of the grain. The radius and nickel content (in weight percent) were then used to determine the metallographic cooling rate using the procedure of Willis and Goldstein (1981), Taylor et al, (1987) and Scott et al. (2014). Nickel contents in taenite were used to determine a closure temperature based on the central nickel taenite method and phase diagram in Reisener and Goldstein (2003a,b), see Figure 2.

Schepker (2014) digitized the phase diagram using Microsoft Excel for ease of computation and this was used to determine closure temperatures. Comparison of the digitized Microsoft Excel phase diagram and published versions of the phase diagram suggest an accuracy of ± 10°C for the calculations of the former.

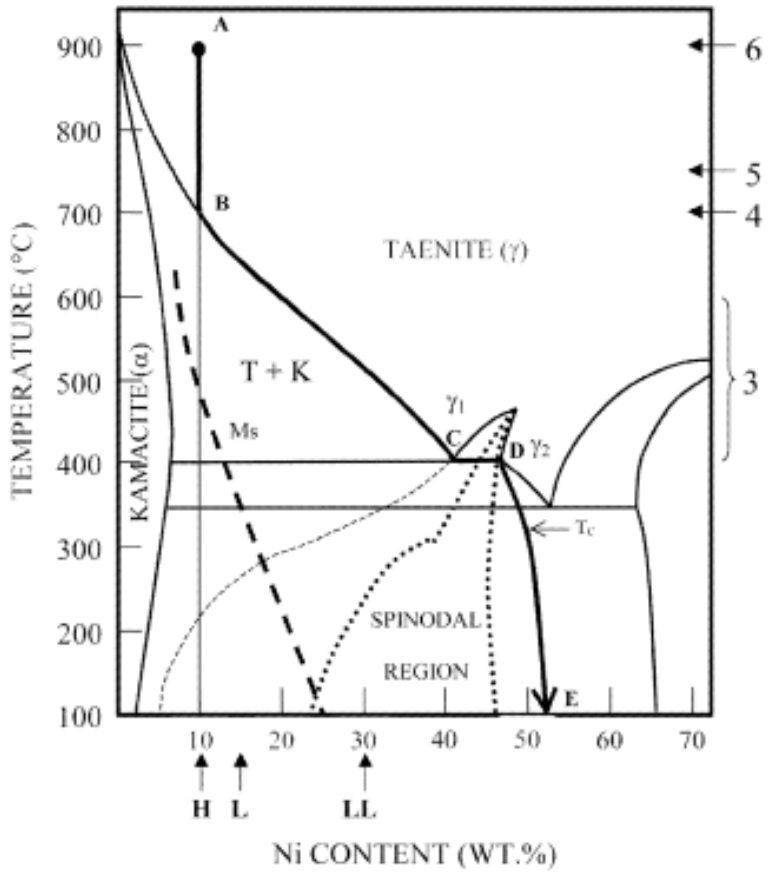

Figure 2. The Fe-Ni phase diagram from Reisener and Goldstein (2003a,b) depicting the taenite Ni compositions and associated temperatures which were used to calculate closure temperatures. The bold path indicates the cooling of a 10% Ni grain through equilibrium conditions. Schepker (2014) digitized the phase diagram using Microsoft Excel to calculate cooling temperatures.

Samples Studied/Classification

Thirty meteorites were examined for the presence of carbide. Table 1 below shows the complete list of meteorites examined as well as the lab numbers and official classifications. The set was selected to sample a variety of ordinary chondrites with variable shock stages for the existence of carbide. Seven were genomict breccias, two

were iron meteorites, three were melt breccias, and two were melt rocks. Melt breccias can include melt-matrix breccias that contain impact melt between constituents, melt breccias that contain significant amounts (approaching 50%) of impact melt, and melt-rich melt breccias that contain mostly impact melt with clasts. According to these definitions, NWA 8709 is a melt-matrix breccia, NWA 5964 is a melt breccia, and NWA 6580 is a melt-rich melt breccia.

Complications

With some exceptions, meteorites listed in Table 1 have the official classifications listed in the Meteoritical Bulletin Database (MBD,). The exceptions are NWA 10454, NWA 5964, and NWA 6580. NWA 10454 has the official classification of L5/6. During further investigation unequilibrated material was found in the main mass that was not visible in thin section. Lower type material, including type 3 and 4, was found during SEM sessions in a newly prepared section. The zoned minerals in Figure 3 confirms the presence of type 3 material. Figure 4 is an example of a melt clast in NWA 10454. For this meteorite, the revised classification is L3-6. The official classification of NWA 5964 is L3-6, however when taking into consideration the abundant melt, L3-6 melt breccia is a more accurate classification. NWA 6580's official classification is L-melt breccia, but a chondritic clast contains both type 3 and 6 material, so NWA 6580 is better described as a type 3-6 melt-rich melt breccia, L-melt (L3-6) breccia is the adjusted classification.

Table 1 All meteorites examined in study

Official Name	CML #	Classification	Shock Stage	Weathering Grade	Classified by Author
San Juan de Allende	0115-0	L3	S3	W1	x
	Allende F				
NWA 7869	0143-1	L3	S3	W1	
NWA 4860	0288-3	L4	S6	W1	
Park Forest	0089-3	L5	S5		
NWA 10455	0153-2B	L6	S4	W2	x
Tenham	0337-2	L6	S5		
Buck Mountains 005	0491-2	L6	S4	W2	
	0491-3A				
Alfianello	0496-1C	L6	S5		
Park	0617-2A	L6	S1		
NWA 11648	0015-2	L6	S5	W1	
NWA 10516	0020-2	L3-6	S5	W1	x
NWA 869	0074-13C	L3-6	S3	W1	
NWA 10454	0139-2	L3-6 *	S4	W1	x
NWA 10517	0142-1	L3-6	S4	W1	x
NWA 10518	0157-2	L3-7	S5	W1	x
NWA 8709	0109-2	L3 Melt Breccia **	S4[1]	W3	x
NWA 5964	0175-4-1	L3-6 Melt Breccia ***	S1-6[1]		
	0175-2A				
NWA 6580	0371-1	L-melt (L3-6) breccia ****	S3[1]	W1	
NWA 6454	0273-1	L-melt rock	Melt	W1	
NWA 6579	0358-1	L-melt rock	Melt	W2	
NWA 3127	0248-B	LL3.10	S2	W3	
Tieschitz	0781A	H/L3.6	S1Δ	W1	
Franconia	0333-1	H5	S3	W2	
Gao-Guenie	0035-14	H5	S2		
NWA 10453	0007-6	H6	S4	W2	x
Kernouve	0666-B	H6	S1		
NWA 11121	0172-3	H3-6	S2ΔΔ	W2	x
Buck Mountain Wash	0144-2B	H3-5	S2	W1	
	0236				
Monteview	0907-1B	Iron, IAB-MG			
Canyon Diablo	USNM1766	Iron, IAB-MG			

* The official classification for NWA 10454 is L5/6, however unequilibrated material was found in the main mass that was not seen in thin section

** NWA 8709 is a L3-melt matrix melt breccia

*** NWA 5964 is chondritic with abundant impact melt

**** NWA 6580 Melt breccia with chondritic clast in melt
Δ Personal Communication with Secana Goudy
ΔΔ Shock classification reported to Nomenclature committee as "low"
[1] Indicates that shock stage is for chondritic portion only

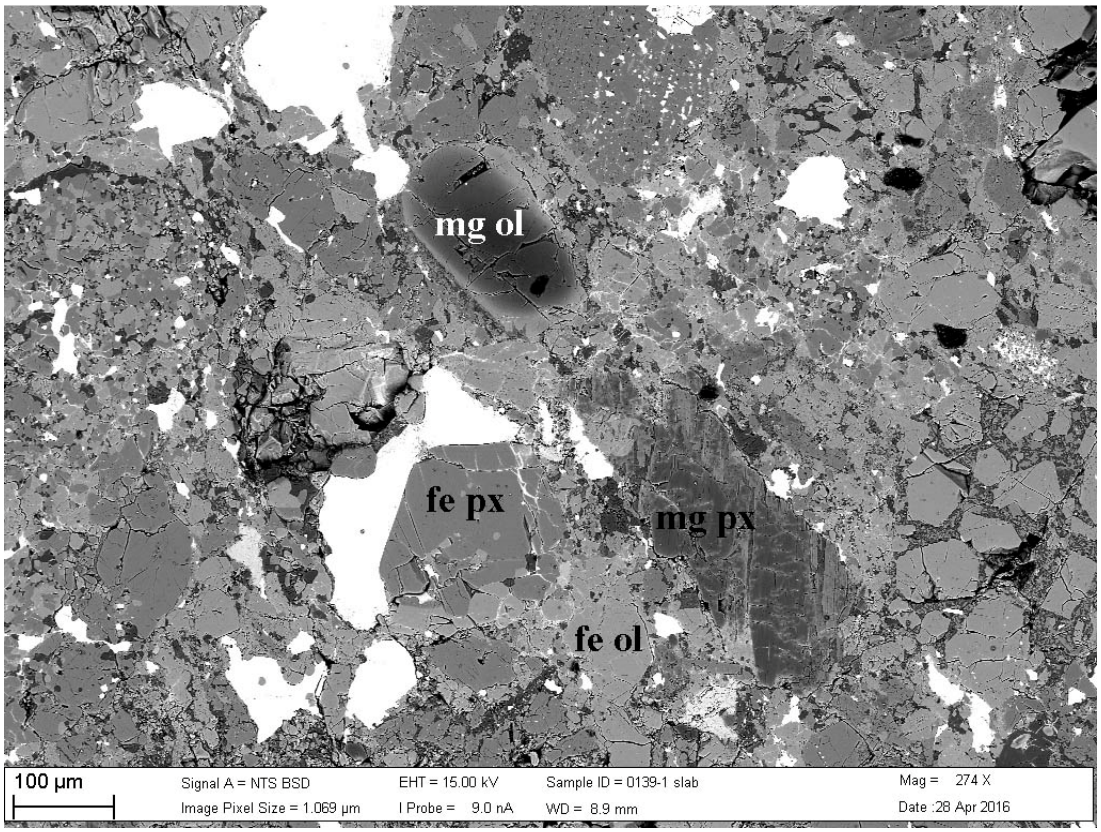

Figure 3. An example of zoned olivine and pyroxene minerals found in a BSE micrograph of NWA 10454 (CML0139-2). The magnesian rich and iron rich versions of pyroxene and olivine have been labeled with "mg" and "fe" accordingly. The image is a classic example for brecciation, in which low type material (mg rich minerals) are heterogeneously mixed with high type material (fe rich minerals). BSE image.

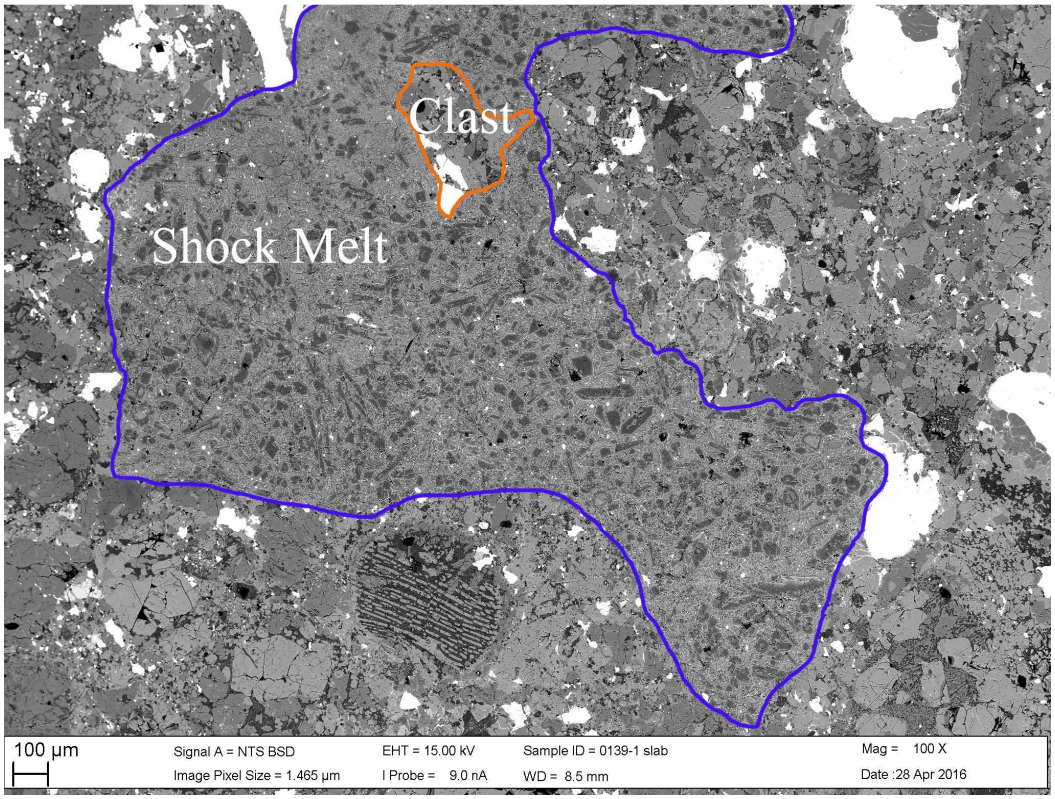

Figure 4. Shock melt in NWA 10454 (CML 0139-2) is visible as the area outlined in blue, surrounded by chondrite areas outside of the blue line and inside of the orange encircled area. BSE image.

Intermeteorite Distribution of Carbide

Shock Characteristics / Brecciation / Melt Zones

Observations over the course of this study have not found carbide in melt, however every carbide bearing meteorite examined has had melt present in the sample. In the case of NWA 10517, there is a shock blackened area, shock melt, and the chondritic host material, Figure 5. No carbide was observed in the melt area, however the shock blackened area had three carbides while the majority occurred in the unmelted chondritic host. The shock blackened area likely received too much heat for carbide formation, or the carbides were destroyed due to too much heat. The shock blackened area contains troilite that mostly rims metal, Figure 6. Both the metal and troilite in the blackened area probably melted. Carbides 27 and 28 in the blackened area likely survived as they occurred in the largest metal grain in the shock blackened area, as can be seen in Figure 5. If the smaller metal grains were melted and remobilized, they could have lost their carbide grains through re-equilibration and that could be why no more carbide grains occur until closer to the chondritic host material. The observations so far indicate that if the melt is too substantial or the temperature too high, the chondritic metal and thus the carbides are destroyed, or prevented from forming.

Regarding brecciation and the distribution of non-carbide bearing and carbide-bearing meteorites, a distinct pattern was observed. With the exceptions of the iron meteorites (as petrographic type and brecciation are not applicable) and San Juan de Allende, all the meteorites that contain carbide are genomict breccias, exclusively those

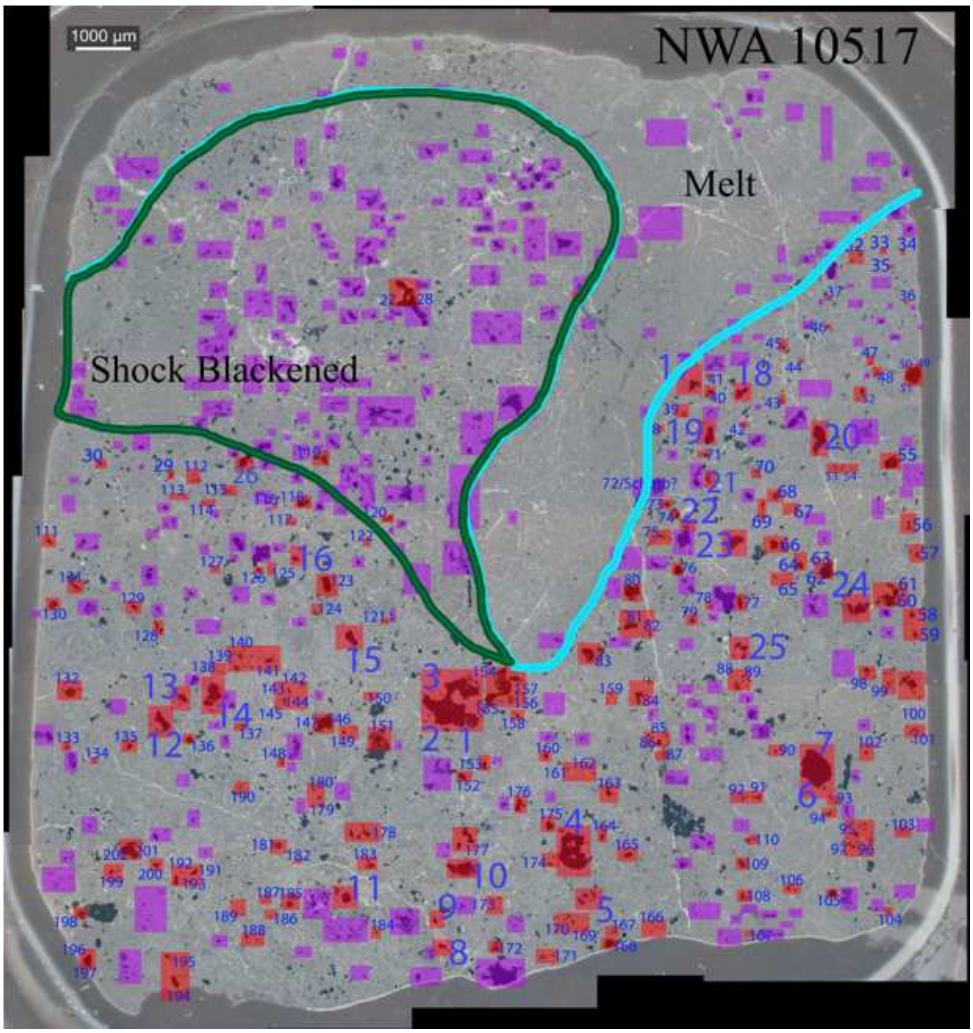

Figure 5.Three distinct textures are present in NWA 10517 (CML0142-1): shock melt, shock blackened material, and the chondritic host. The red boxes denote the presence of carbide and the blue number its photo designation, the purple boxes denote the absence of carbide in an area. No carbides occur in the melt area and only three were found in the shock blackened area. The carbides primarily occur in the chondritic host, near but not in the shock melt. Base image: inverted reflected light.

that contain type 3 material, Figure 7. San Juan de Allende is a type 3 meteorite and does contain carbide. The non-carbide bearing meteorites sample a range of petrographic types, but no carbide was found in the higher types without the presence of type 3 material. The type 3 material was always present in meteorites that were observed to contain carbide.

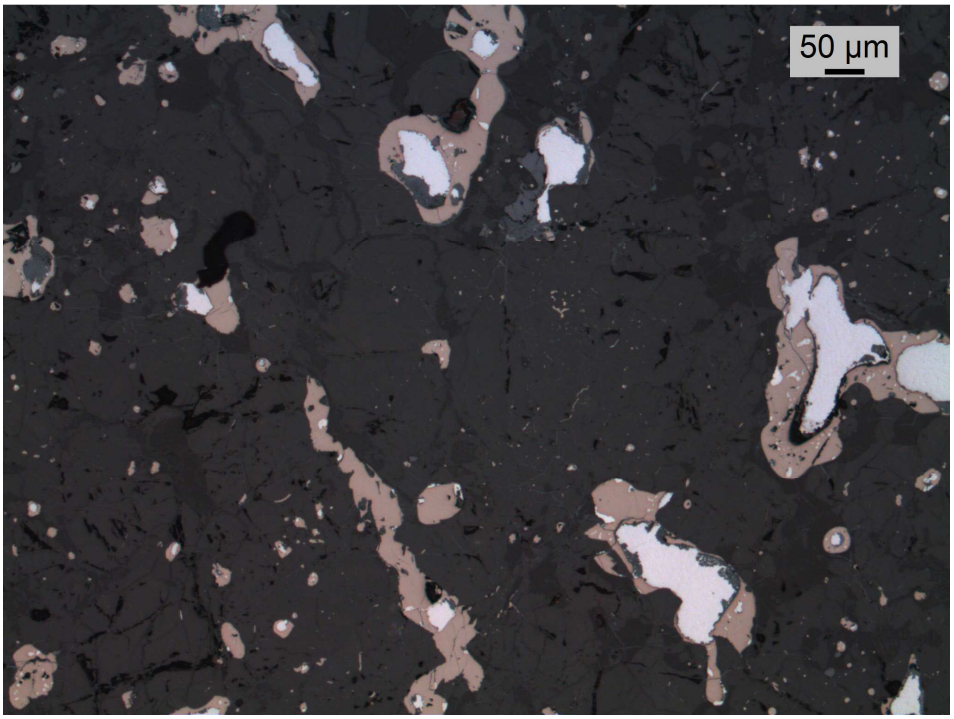

Figure 6. Troilite (tan) mainly surrounds metal (white) in NWA 10517 probably as a result of metal-troilite melting. Photo 0142-anom-metal texture 02, thin section CML0142-1. Reflected light image.

Shock stage was also examined for a correlation with the presence of carbide. See Figure 8. The carbide bearing meteorites, with respect to shock stage, exhibit almost a bell curve distribution (Figure 8a), however, no relationship with the presence of carbide was found.

The relationship between shock, melt zones, and the presence of carbide is complicated. In the case of NWA 8709, an L3-melt matrix melt breccia, the matrix was melted, leaving the chondrules mostly intact but deformed. Olivine indicated a shock stage of S4 (Ruzicka et al., 2015). No carbide was found in the sample. NWA 6580 is an L melt breccia that contains a L3-6 clast that did not experience melting. No carbide was found in the melt; however, it was found to occur in the unmelted L3-6 clast (Schepker,

2014). NWA 5964 is a L3-4 melt breccia, roughly half melted with a chondritic portion that did not melt. Once again, carbide was not found in the melt but was present in the unmelted chondritic portion (Hauver and Ruzicka, 2011, Schepker, 2014).

Distribution of Carbides with Respect to Lithology

The spatial distribution of carbide varies across textures within individual meteorites as well as between different meteorites. Table 2 is the breakdown of the number of carbide grains found per meteorite and in what lithology they were found in. The total number of metal grains that were examined for carbide and the number of carbide grains found are given. The proportion of carbide against the total amount of metal grains examined is given, in addition, the proportion of carbide found in each type of lithology is also given in the same column. Host material and low type material are the primary textures that carbide can be found in, with smaller occurrences in shocked (but not melted) areas and low-type clasts. Higher-type clasts within genomict breccias occasionally host carbide, but the amount of carbide in such clasts is small. Melt has not been observed to contain carbide.

The more complicated lithologies of NWA 10518 and NWA 11121 can be seen in plane polarized light in Figure 9 and Figure 10, respectively. NWA 10518 has three main lithologies; the host, the two high type clasts (A and B), and the shock melt (S). The melt and smaller clast “B” had no carbide. The large clast, “A”, had 14 carbides, which amounted to 2.5% of the total amount of carbides. The host had the majority of the carbides at 97.5%, or 549 carbides. NWA 11121 (Figure 10) contains three lithologies; host material, two low type clasts (D and E), and three high type clasts (A, B, C) of which

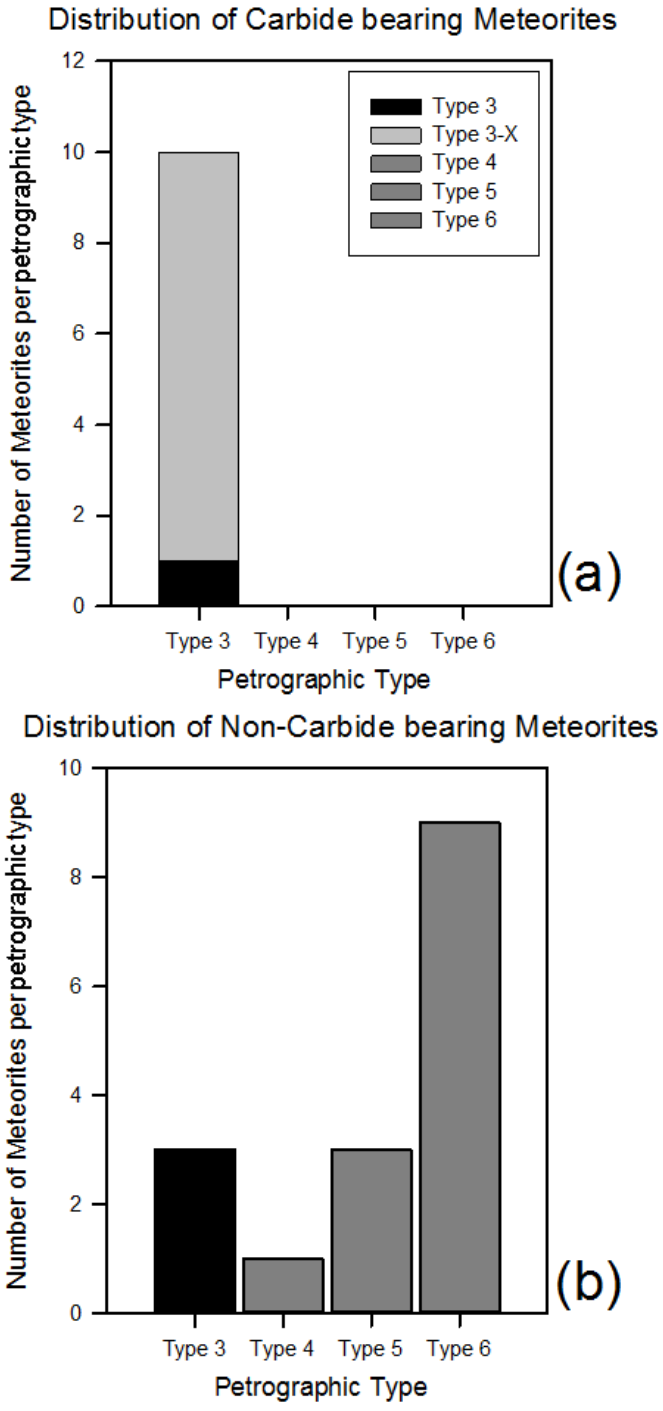

Figure 7. The distribution of meteorites by petrographic type is illustrated above. Plot (a) shows the distribution for carbide bearing meteorites, Type 3-X indicates genomict breccias and plot (b) is for non-carbide bearing meteorites.

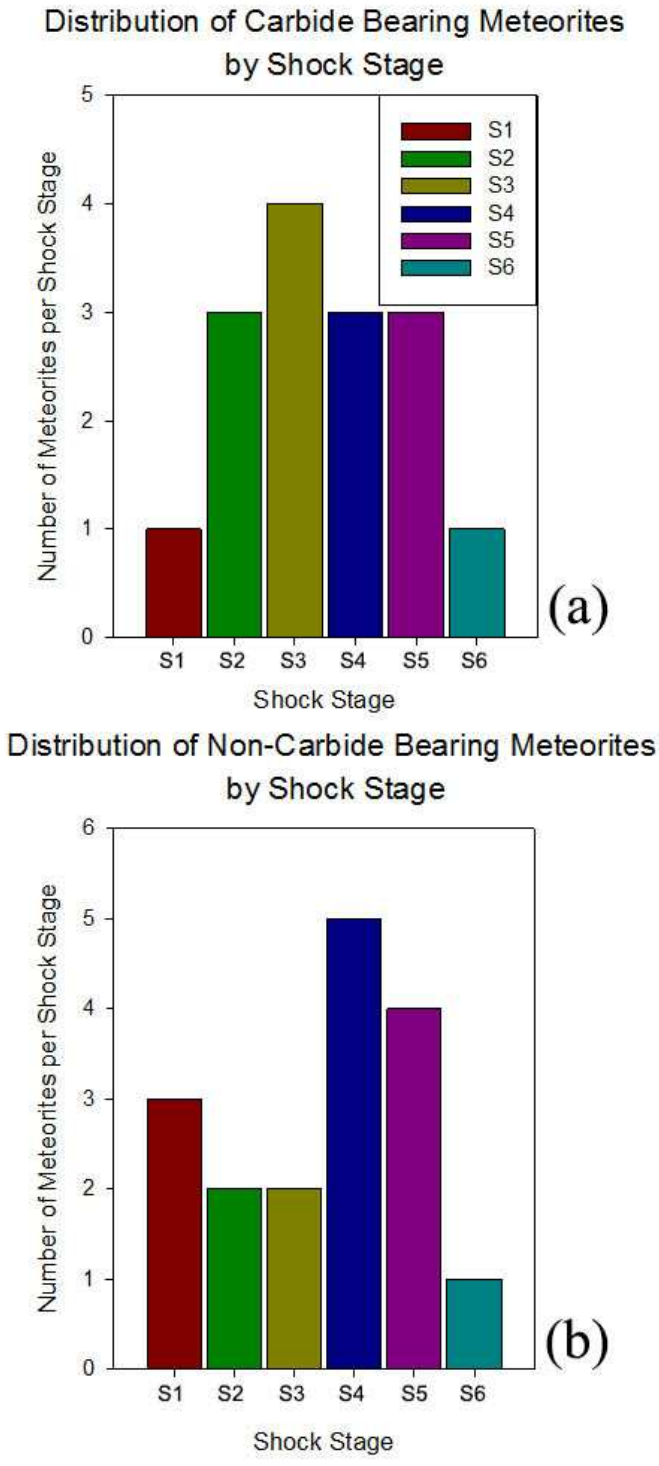

Figure 8. The distribution of meteorites by shock stage is shown above. Plot (a) shows the carbide bearing meteorites and plot (b) shows the non-carbide bearing meteorites.

Table 2 Distribution of carbide grains by lithology

Official Name	Carbide (Y/N)	Number of Metal Grains Examined	Number of Carbide Grains Found	Proportion of Carbide (%)	Silicate Shock Melt
Buck Mountain Wash (0144-2B)	**Y**	1292	833	64.5	Y
Mixed Lithology			116	13.9	
Type 3			717	86.1	
Buck Mountain Wash (0236)	**Y**	677	30	4.4	Y
High Type			0	0	
Mixed Lithology			30	100.0	
NWA 869 (0074)	**Y**[1]	283	277	97.9	Y
Host			275	99.28	
Melt			0	0.0	
Shock Blackened			2	0.72	
NWA 5964 (0175-4-1/0175-2A)	**Y**[2]	401	372	92.8	Y
NWA 6580 (0371-1)	**Y**[3]	79	26	32.9	Y
NWA 10454 (0139-2)	**Y**	318	77	24.2	Y
NWA 10516 (0020-2)	**Y**	464	155	33.4	Y
NWA 10517 (0142-1)	**Y**	481	202	42.0	Y
Host			198	98.0	
Shocked Area			4	2.0	
Shock Melt			0	0.0	
NWA 10518 (0157-2) *	**Y**	1315	563	42.8	Y
Host			549	97.5	
Clast A			14	2.5	
Clast B			0	0.0	
Melt			0	0.0	
NWA 11121 (0172-3) **	**Y**	2480	153	6.2	Y
Host			127	83.0	
Clast A			0	0.0	
Clast B			0	0.0	
Clast C			7	4.6	
Clast D			19	12.4	
Clast E			0	0.0	
San Juan de Allende (0115-0)	**Y**	292	85	29.1	Y
Monteview (0907)	**Y**				
Canyon Diablo (USNM 1766)	**Y**				

[1] Data courtesy of M. Hutson

[2] Data courtesy of M. Hutson, K. Hauver and L. Likkel

[3] Data courtesy of K. Hauver

*Clast A is a large high type clast, Clast B is a small high type clast

** Clast A,B, and C are high type clasts, Clast D and E are low type clasts

only "C" contains carbide. Of the low-type clasts, only "D" contained carbide, while most of the carbide was found in the host material.

As Table 2 illustrates, carbide can primarily be found in the host material or in the mixed lithologies containing type 3 material. The host material of the breccias contain fragments from the petrographic types of material that make up the meteorite (Bischoff et al., 2006), which for the carbide bearing meteorites are type 3-6, with the exception of San Juan de Allende. High-type clasts tend to be either void of carbide or contain only small amounts. While melt does not contain carbide, areas in close proximity to melt can contain carbide, such as shock blackened areas but generally not as much as the host material (Figure 5).

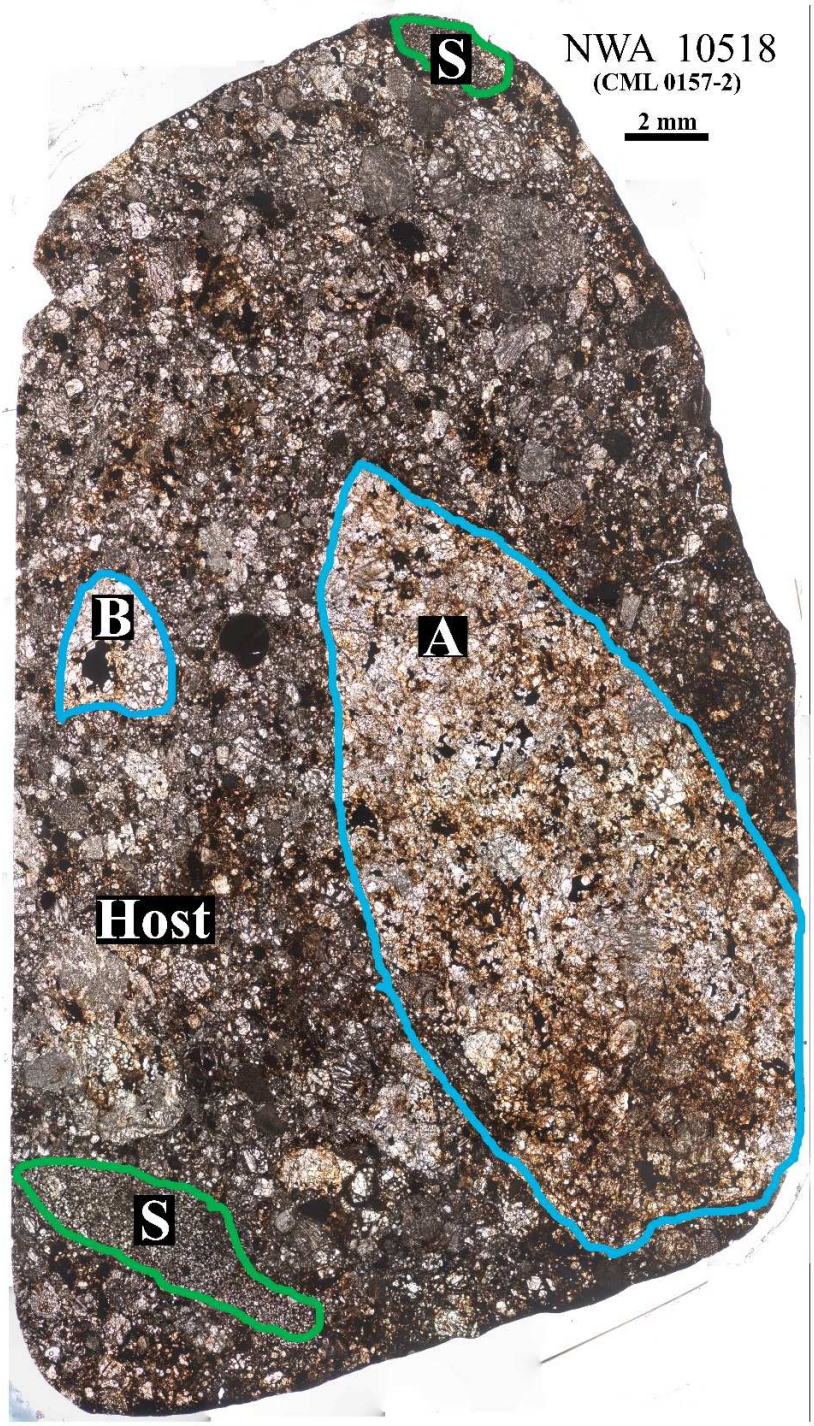

Figure 9.The lithologies of NWA 10518 (CML0157-2) can be seen above. The two clasts outlined in blue and labeled "A" and "B" are high type clasts, with the larger clast being type 6 material. The two areas in green and labeled with "S" are shock melt. The rest of the thin section is considered the host material. Plane-polarized transmitted light image.

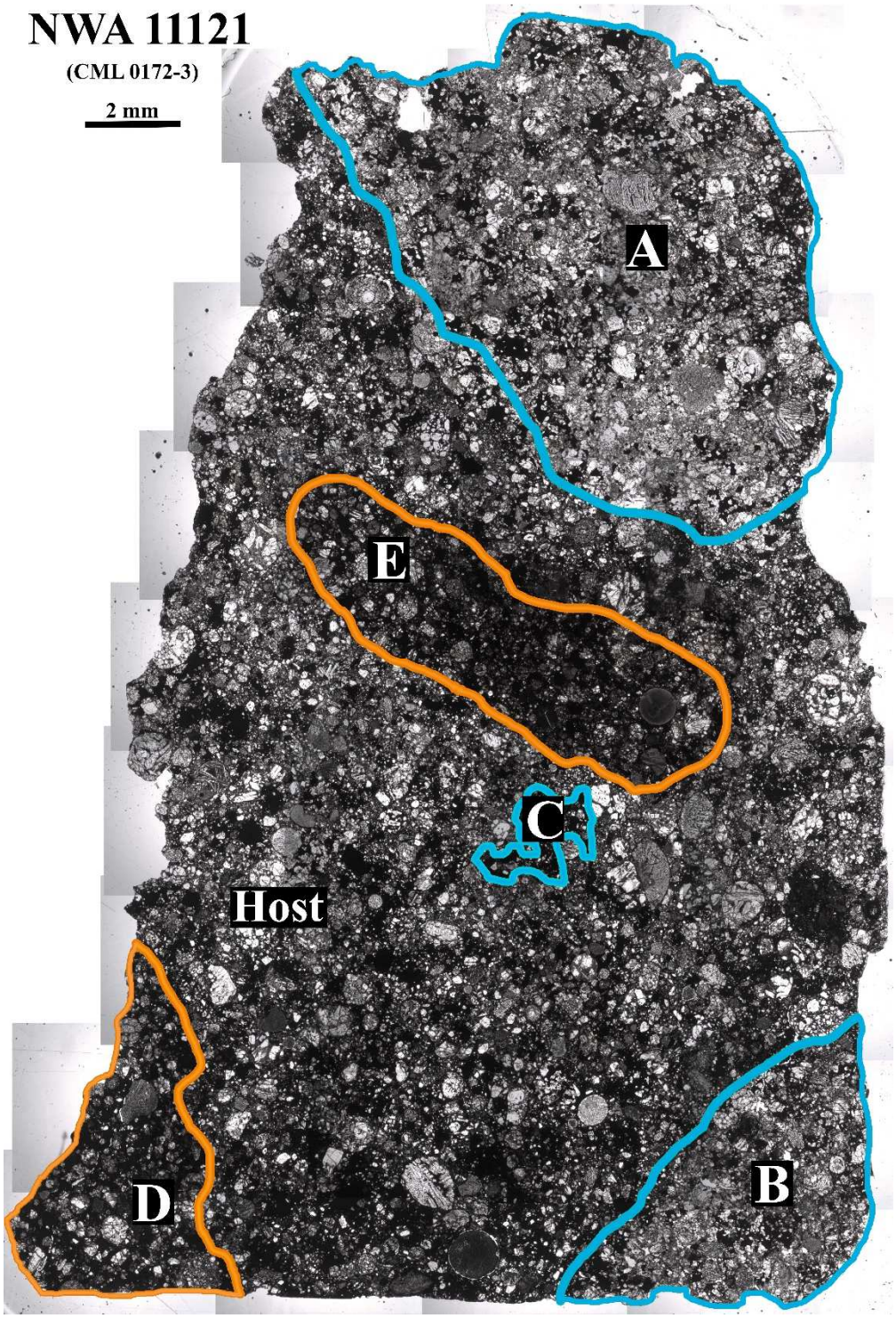

Figure 10. The lithological breakdown of NWA 11121 (CML 0172-3). The blue areas "A", "B", and "C" are high type clasts and the orange areas, "D" and "E" are low type clasts. Plane-polarized transmitted light image.

Intrameteorite Distribution of Carbide

The distribution of carbide within a thin section varies from meteorite to meteorite and there is heterogeneity, or variations, within a given meteorite. As discussed previously, NWA 11121 contains five clasts, three high type clasts (A, B, C) and two low type clasts (D, E), in addition to the host material, Figure 10. The locations of carbide bearing metal grains are added in Figure 11. Two of the high type clasts do not contain carbide and only the smallest (C) contains seven carbide grains. These carbides are located entirely on what appears to be the edge of the clast. Of the two low type clasts, only D contained carbide. It can be inferred that type 3 material alone is not enough for the formation of carbide as not every type 3 clast contains carbide. Additionally, NWA 11121 displays a heterogeneous distribution of carbide in the host material. The carbides cluster loosely together in several areas, i.e. to the left of clast A, above clast B, to the right of clast D, and to the left of clast C (Figure 11). Otherwise they are dispersed more sparsely through the rest of the host material with larger areas containing fewer carbides than the clusters.

Figure 12 illustrates the carbide distribution in NWA 10518. Other than the host material, there are two high type clasts (A, B) and two patches of shock melt (S) present in thin section. Of the four areas, only one of the high type clasts contains carbide, marked “A” on Figure 12. Clast A has 14 carbides, most of which occur near the boundaries of the clast. NWA 10518 has a more homogenous distribution of carbide when compared to NWA 11121 in regard to the host material. While there are no visible clusters, there are two small areas in the host that contain no carbide. This includes an

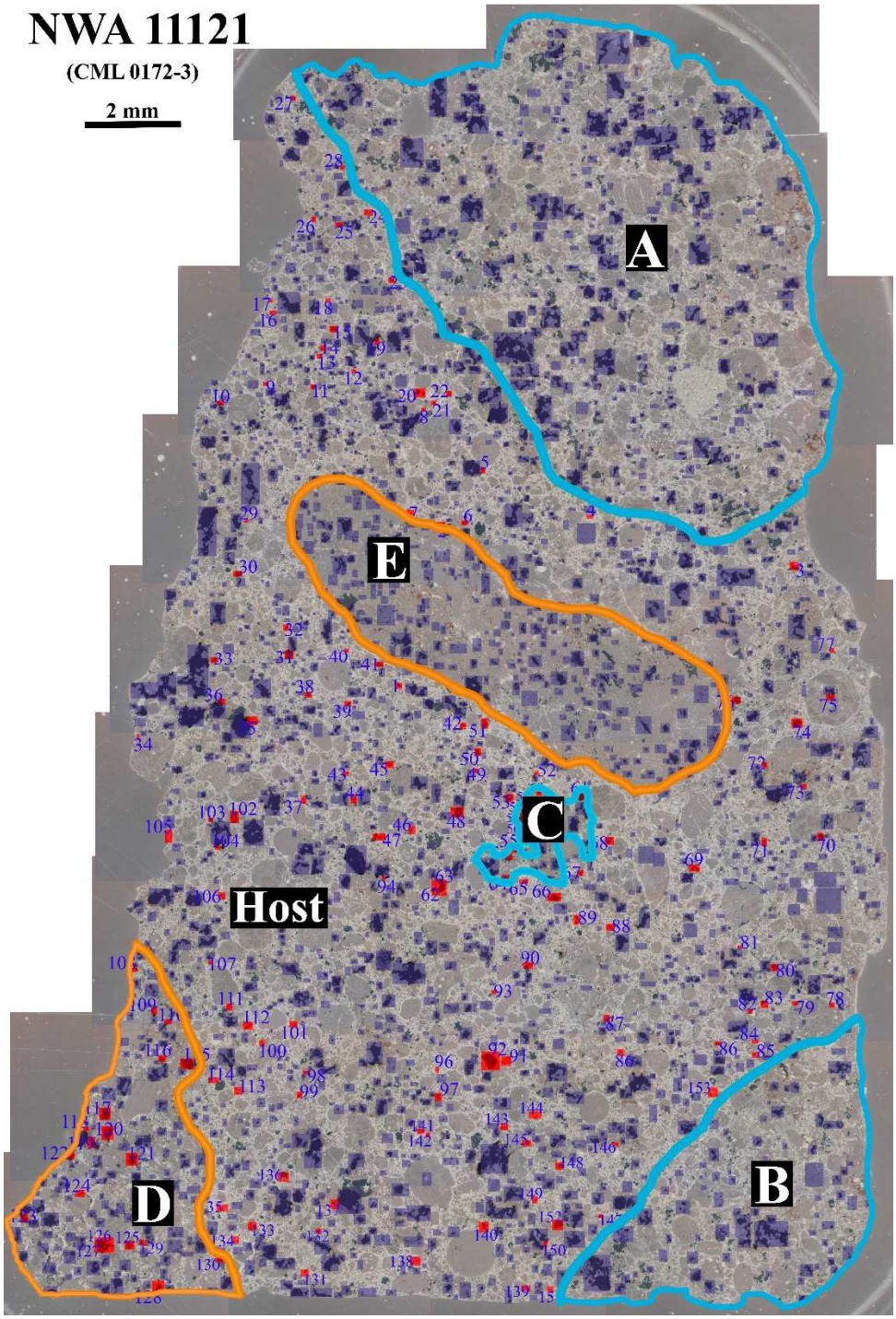

Figure 11. Carbide distribution map of NWA 11121 (CML0172-3). Carbide locations are marked in red boxes while the dark purple boxes mark non-carbide bearing metal grains. The three high-type clasts are denoted using "A". "B", and "C" while the low-type clasts are labeled "D" and "E". The host material is marked accordingly. Base image: inverted reflected light, image color enhanced.

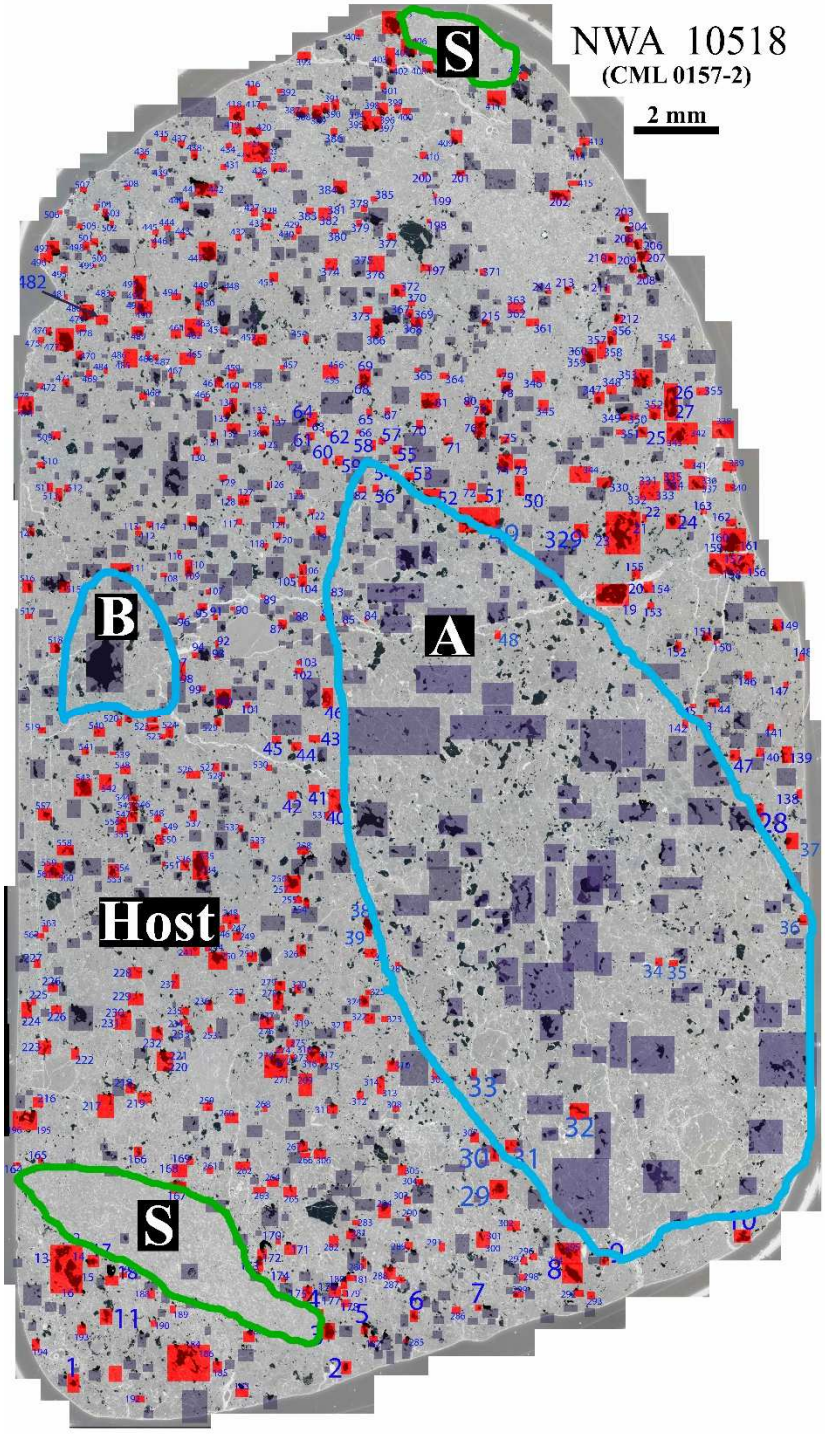

Figure 12. Spatial distribution of carbides in NWA 10518 (0157-2). Carbide locations are marked in red boxes while the dark purple boxes mark non-carbide bearing metal grains. The two high-type clasts are denoted using "A" and "B" and the shock melts are labeled "S". The host material is marked accordingly. Base image: inverted reflected light, image color enhanced.

area approximately two millimeters below the upper shock melt in an area devoid of metal, and an area about one millimeter above clast B (Figure 12).

The carbide distribution of Buck Mountain Wash in regard to lithology is shown in Figure 13. The left side of the thin section (A) is mixed lithology, containing both high and low-type material while the right (B) is just type 3 material. The mixed lithology also contains a patch of shock melt, outlined in green, which contains no carbide. The low type material on the right contains many carbide grains. Few metal grains were found to contain no carbide. The mixed-type lithology contains far fewer carbides, arranged in a more heterogeneous distribution, which has no visible correlation to the boundary between the two textures (cyan line). There are two clusters of carbides, one to the left of the shock melt and the other below the shock melt, close to the boundary.

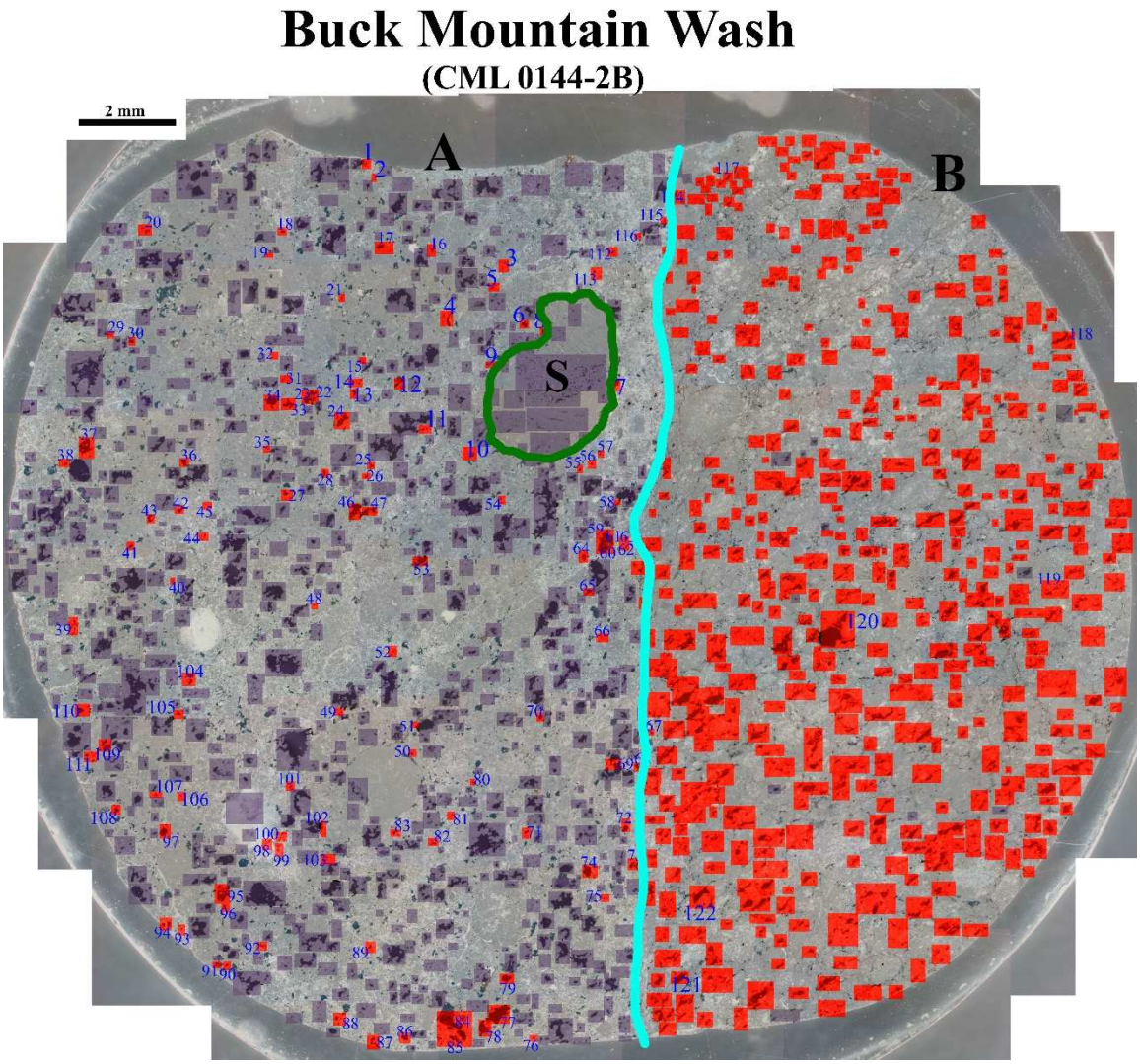

Figure 13. Buck Mountain Wash (CML 0144-2B) illustrates a striking example of the spatial distribution of carbide. Carbide locations are marked in red boxes while the dark purple boxes mark non-carbide bearing metal grains. On the right is the low type lithology (B) that is dominated by the presence of carbide. The mixed lithology on the left (A) contains fewer carbides. The mixed lithology on the left also contains shock melt (S) that contains no carbide. Base image: inverted reflected light, image color enhanced.

Textures and Mineralogy

Many of the metal grains that host carbide are plessite, a mixture of both kamacite and taenite within a metal grain. Three categories were used to describe the textures of the kamacite and taenite mixtures that contained carbide. These are fine plessite, coarse plessite, and blocky intermixture. Three additional categories were used for when none of the previous named mixtures were applicable: these were largely kamacite, largely taenite, and largely carbide (Figure 14).

Fine plessite was categorized as a fine-grained intermixture of kamacite and taenite where the space in between the taenite lathes was five microns or less, Figure 14d. Coarse plessite was much the same except that the space between the taenite grains was greater than five microns, Figure 14e. Figure 14f is a texture called blocky, where kamacite and taenite are still both present in large amounts in the metal grain but kamacite and taenite exist as more globular structures and each mineral is larger than what is seen in plessite.

The largely kamacite, largely taenite, and largely carbide textures (Figure 14a, b, and c respectively) were used when no other mineral phase are present in any significant amount. Figure 14a is an example of largely kamacite where the red circles are marking small taenite grains. Since the amount of taenite is miniscule in relation to the kamacite, and neither of the three textures involving both kamacite and taenite describe the texture, this is called largely kamacite. Figure 14b

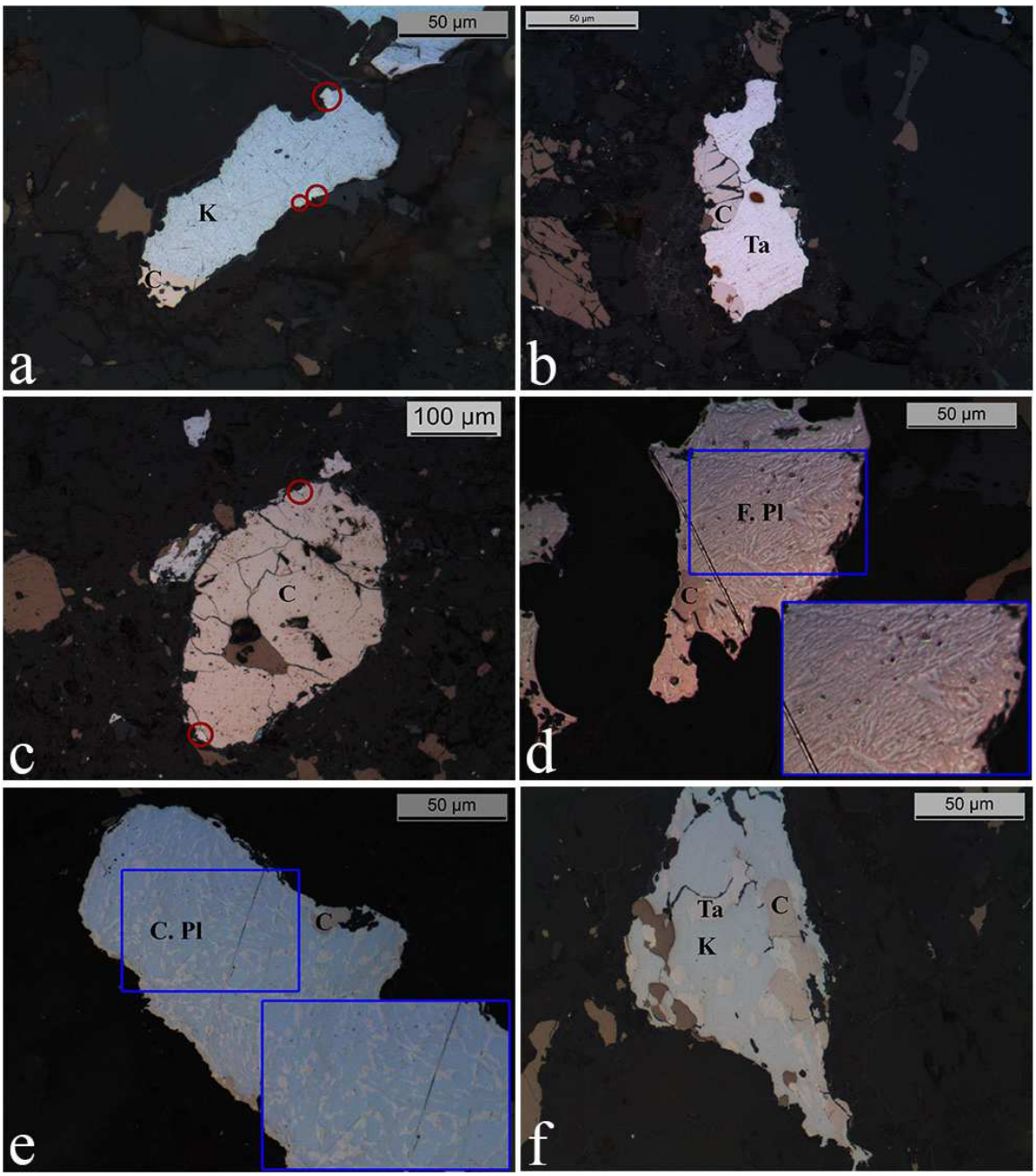

Figure 14. The six metal textures observed to host carbide are pictures above. C = carbide, K = kamacite, Ta = taenite, F. Pl = fine plessite, C.Pl = coarse plessite. A: largely kamacite, the red circles indicate small taenites, which while present are not enough to count the grain as another texture. Image from NWA 10516 (CML0020-2), photo designation 0020-2-C-12. B: largely taenite. Image from NWA 11121 (CML0172-3), photo 0172-3-C-71. C: largely carbide, the red circles indicate small taenites. This grain is also the largest carbide found yet. Image from Buck Mountain Wash (CML0144-2B), photo 0144-2B-C-037. D: fine plessite, the distance between the taenite lathes is 5 microns or less. Image from NWA 10454 (CML0139-2), photo 0139-2-Carbide-52. E:

coarse plessite, the distance between the taenite lathes is greater than 5 microns. Image from NWA 10517 (CML0142-1), photo 0142-1-C-152. F: blocky, the intermixture of kamacite and taenite are larger than plessite and have a more globular, blocky look. Image from NWA 10518 (CML0157-2), photo 0157-2-C-513. Images have been color enhanced. All images reflected light, color enhanced.

is the equivalent but for taenite. Other than the carbide, there is no other metal seen, so it is largely taenite. Lastly, Figure 14c is largely carbide. The two red circles are small taenite grains while the rest of the grain is carbide. This is also the largest carbide grain (~375 x 200 microns) found during this study.

The number of carbide grains found per metal texture was also examined, Table 3. For each meteorite thin section, the number of carbide photos and its percentage is given for each textural type with the total in the last column on the right. With the exception of NWA 10454, coarse plessite grains are relatively rare in occurrence compared to other textural types, with an abundance of less than 10 percent. Largely carbide is similar, where the percentages of occurrence is usually less than three percent, with the exception of Buck Mountain Wash and NWA 11121, which respectively have occurrence percentages of 16.9 and 42.5. Most often, carbide is primarily found with both kamacite and taenite present in the same grain, either in the form of fine plessite, coarse plessite, or blocky grains. These texture types comprise ~67-75% of the metal grains associated with carbide in NWA 10516, NWA 10454, NWA 10517, and NWA 11121 (Table 3).

An exception is NWA 11121, which has most of its carbide occurring in largely carbide, largely kamacite, and largely taenite textures. Buck Mountain Wash is similar;

however, it has a large portion of carbide occurring in the blocky mixture between kamacite and taenite.

Table 3. The occurrence of carbide by the texture of the host metal.

Meteorite	Blocky Mixture	Largely Kamacite	Largely Carbide	Plessite Coarse (>5 mic)	Plessite Fine (<5 mic)	Largely Taenite	Totals
NWA 10516	39	28	1	8	74	8	158
	24.7	17.7	0.6	5.1	46.8	5.1	100.0
San Juan de Allende	37	18	2	1	1	30	89
	41.6	20.2	2.2	1.1	1.1	33.7	100.0
NWA 10454	4	16	1	14	39	3	77
	5.2	20.8	1.3	18.2	50.6	3.9	100.0
NWA 10517	40	39	0	8	97	21	205
	19.5	19.0	0.0	3.9	47.3	10.2	100.0
Buck Mountain Wash	27	38	21	7	8	23	124
	21.8	30.6	16.9	5.6	6.5	18.5	100.0
NWA 10518	137	117	7	53	194	65	573
	23.9	20.4	1.2	9.2	33.9	11.3	100.0
NWA 11121	20	29	65	5	11	23	153
	13.1	19.0	42.5	3.3	7.2	15.0	100.0

Figure 15 illustrates the occurrence of carbide by textural type of host metal. The amount of carbide that occurs in largely kamacite is roughly the same across all seven samples. Largely taenite, fine plessite, and largely carbide vary widely across the different meteorites. Coarse plessite has a lower occurrence rate than the other host metal textures, as stated previously, and so it does not vary as much as some textures. The blocky textures do vary, but like the coarse plessite, they do not vary as much as other textures. However, unlike coarse plessite, it frequently represents a larger portion of the occurrence of carbide. Blocky, fine, and coarse plessite represent different intergrowth scales and nucleation between taenite and kamacite, and carbide occurs in all three

textures to various degrees. When plessite is present, carbide is found dominantly in the fine plessite over the coarse plessite. There is a general anticorrelation between blocky and total plessite regarding the presence of carbide. San Juan de Allende has almost no plessite hosting carbide, but it has the largest percentage of blocky texture hosting carbide. In NWA 10454, which has the most plessite, there is the least amount of blocky texture.

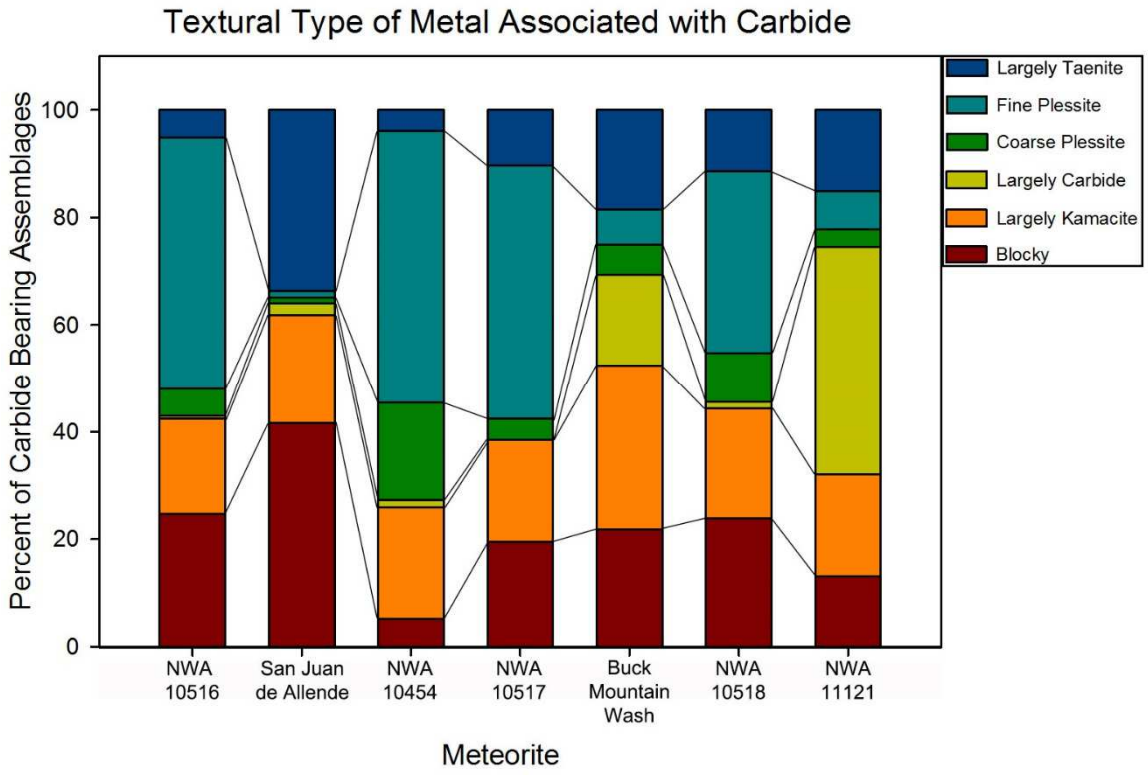

Figure 15. The distribution of carbide with respect to the texture of the host metal, in percentage of occurrence.

The location of carbides in their host metal was also examined. The total number of carbide grains in three meteorites were examined for their position in each metal grain. The two possible positions were inside the host metal and on the edge of the host metal.

The results are listed in Table 4. The numbers are presented in percentages while the total number of carbides in the meteorite is given by "N". These numbers differ from the previous graph because every carbide in each photo was individually counted rather than each photo being considered as a whole. Carbides are predominantly found on the edge of metal grains. Carbide grains found on the inside of metal grains, are always in contact with another mineral phase or a fracture. This is consistent with the highest percentages of carbides found on the inside of grains being in fine plessite and blocky textured metal grains, both of which have multiple kamacite-taenite interfaces deep within metal grains. Carbides are not observed to occupy space inside of a metal grain without being in contact with another phase or fracture.

Carbides can exhibit euhedral, subhedral, and anhedral shapes. The carbide grains tend to be subhedral, with several crystal faces visible, however there are carbide grains that are anhedral lack crystal faces. The occasional euhedral carbide has also been observed. Figure 16 has two carbides that illustrate the subhedral and anhedral textures. The subhedral grain marked C2 has several prominent crystal faces marked by white arrows while the rest of the grain has no distinct crystal faces and is rather smooth and irregular in shape. C1 is an anhedral grain, it is smooth and irregular in shape with no visible crystal faces. An example of a euhedral carbide grain can be seen in Figure 17. It has distinct crystal faces on all six sides of the grain and appears symmetrical. Very few euhedral carbide grains have been found.

Several additional features have been observed in carbides. These are taenite rimming, troilite intergrowths, budding texture, anhedral formations, and carbide-

magnetite assemblages. Regarding taenite rimming, it has been observed that taenite will occasionally form a thin rim on the edge of carbide grains. Taenite rims on carbides have been mentioned by Fang et al., (2010). During this study, the taenite rims were observed to occur in all meteorite samples except for San Juan de Allende. The frequency of the taenite rims is not uncommon; however, it does vary from meteorite to meteorite. NWA 10454 had only one observed taenite rim while NWA 10518 had 150 occurrences.

Table 4. Occurrence (%) of carbide by position in host grain

		NWA 10516 (0020-2)	NWA 10518 (0157-2)	Buck Mountain Wash (0144-2B)
Largely Kamacite	Edge	13.4	13.6	17.0
	Inside	0.0	0.2	2.9
Largely Taenite	Edge	2.4	6.6	11.1
	Inside	0.3	0.5	0.7
Plessite Fine (<5 um)	Edge	37.3	35.9	4.4
	Inside	20.1	9.4	0.2
Plessite Coarse (>5 mic)	Edge	4.0	7.9	3.4
	Inside	0.5	3.0	7.1
Blocky Texture	Edge	18.0	19.0	17.9
	Inside	3.2	2.0	21.6
Largely Carbide	Edge	0.5	1.8	13.0
	Inside	0.3	0.0	0.5
All types	Edge	75.6	84.8	66.8
	Inside	24.4	15.2	33.2
	Total %	100	100	100
	N	373	1564	407

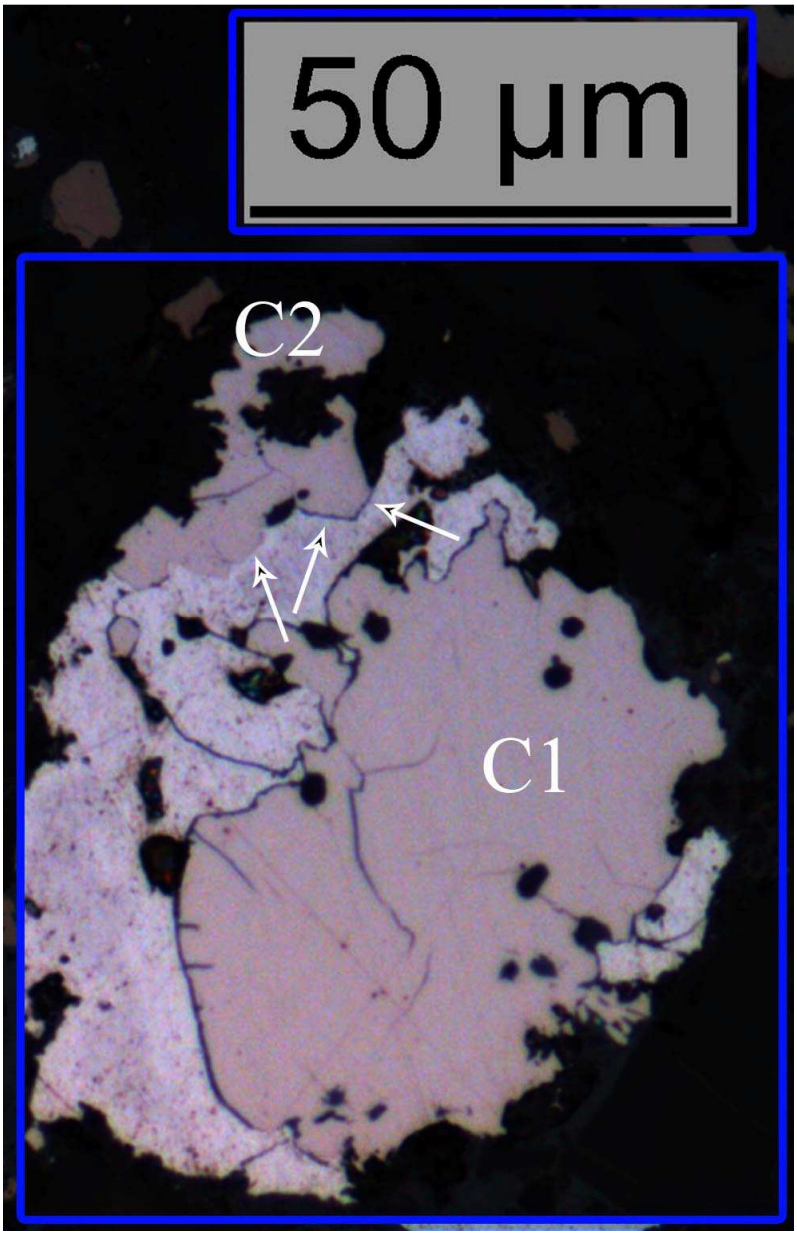

Figure 16. Subhedral and anhedral textures can be observed above in NWA 11121 (CML0172-3), inset from photo 0172-3-C-20. C1 illustrates an anhedral texture, where the edges of the carbide are smooth, rounded, and misshapen. C2 is a subhedral grain, several sharp crystal faces are pointed out by the arrows while the rest of the grain lacks the crystal faces. Reflected light image, color enhanced.

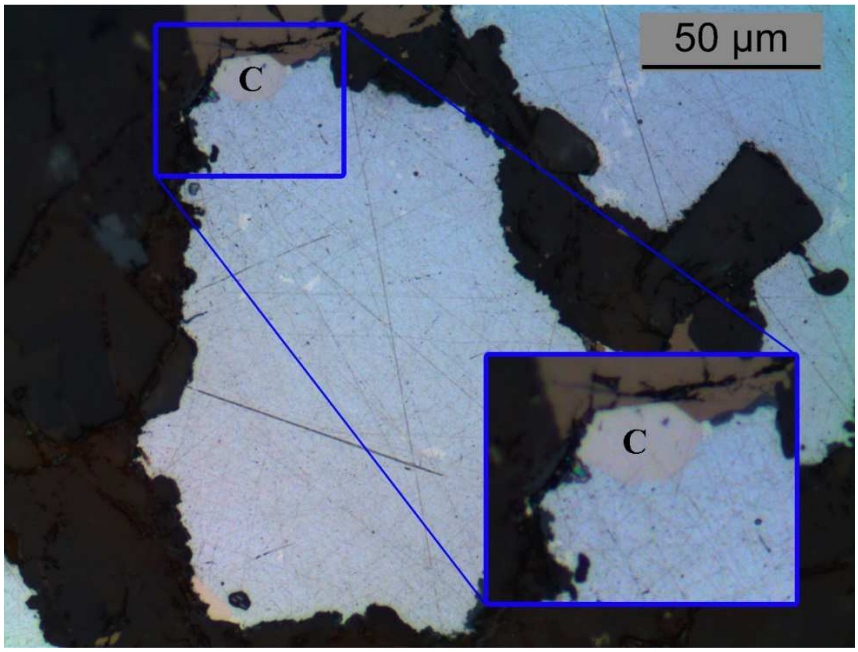

Figure 17. The carbide grain labeled "C" is an example of a euhedral grain found in NWA 10516. Photo 0020-2-C-44 (thin section CML 0020-2). Reflected light image, color enhanced.

Figure 18 and Figure 19 illustrate the taenite rims on carbide minerals. In Figure 18, the carbide grain C1 has a taenite rim along much of its length, the black arrows point out prominent parts of the rim. There are parts of C1 that do not have a taenite rim. As carbide grains frequently occur on the edge of metal grains, it would not be possible for the carbide to be entirely surrounded by a taenite rim in such cases. Additionally, there are parts of the carbide grain that face into the metal that do not have a taenite rim. Therefore, a carbide was considered to have a taenite rim if part of the carbide had a thin layer of taenite while kamacite was on the other side of the taenite. If a carbide is surrounded by thick taenite layers or the carbide occurred in a largely taenite grain, this was not considered a taenite rim.

Figure 19 has additional examples of the taenite rims. Black arrows indicate prominent parts of the taenite rim. In Figure 19A, the large carbide on the inside of the metal grain has large areas where there is no taenite rim before the rim appears in irregular intervals. For the carbide on the upper left, only the inner facing side is considered to have a taenite rim as the taenite is too thick near the edge to be regarded as rim. The carbide is an excellent example of a taenite rim as it follows for much of the length as the grain wraps around, forming a rough bridge in shape. Figure 19B has a carbide in the center that is an example of irregular taenite rims. Only small parts of the grain have the taenite rims but as they are still visible as thin rims of taenite. The carbide is still considered to have a taenite rim, especially given the presence of additional taenite rims with the carbides to the bottom and left.

Troilite intergrowths associated with carbide are an additional feature seen in some meteorites. Not as common as the taenite rims, the troilite intergrowths generally occur inside of the metal grains, rather than on the edges. Figure 20 and Figure 21 are representative examples of some of the troilite intergrowths seen during this study. The troilite appears inside of the metal in irregular, globular grains. Troilite is present as an adjacent grain at the edges of the metal grain when the troilite particles are inside of the metal.

These observations are consistent with an investigation by Tomkins (2009) that identified the relationship between the troilite inclusions in metal and shock. Tomkins (2009) found that the irregular heating from the shock wave propagation could account

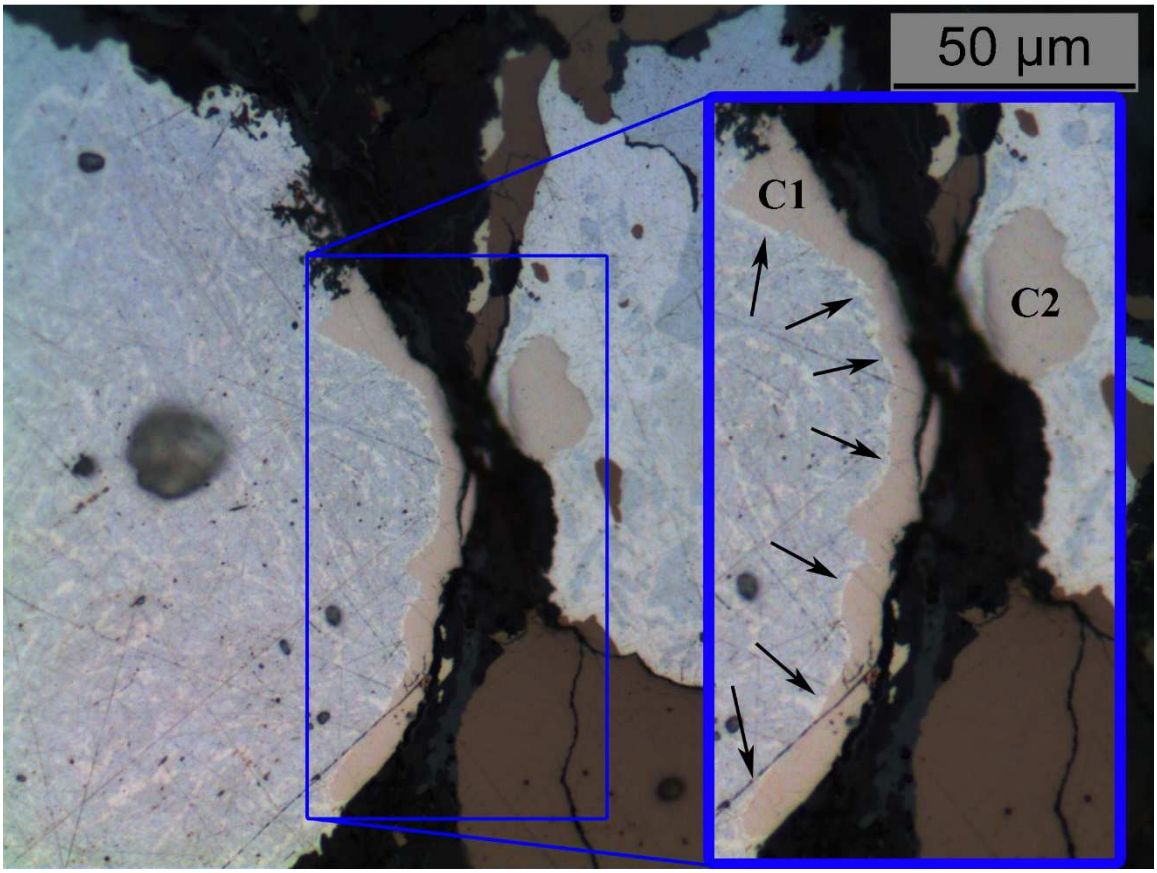

Figure 18. Example of a taenite rim (cream-colored) on carbide C1 from NWA 10516. Carbide C2 is an example of a subhedral carbide grain where several crystal faces can be seen. This carbide image has the designation 0020-2-C-108. Reflected light image, color enhanced.

for the troilite inclusions. Sulfur from the troilite on the outside of the metal is liberated by heat and diffuses into the metal. This has the net effect of small amounts of troilite forming inside of the metal. Tomkins (2009) gives an upper limit of 911°C for this process to occur, due to the solubility of sulfur. He argues that shock is most likely to produce the troilite inclusions because it accounts for the irregularity of the inclusions in meteorites and thin sections, produces enough heat to liberate the sulfur without melting the silicates or other metals, and can cause flaws in the metal that allow the sulfur to diffuse farther into the metal (Tomkins 2009).

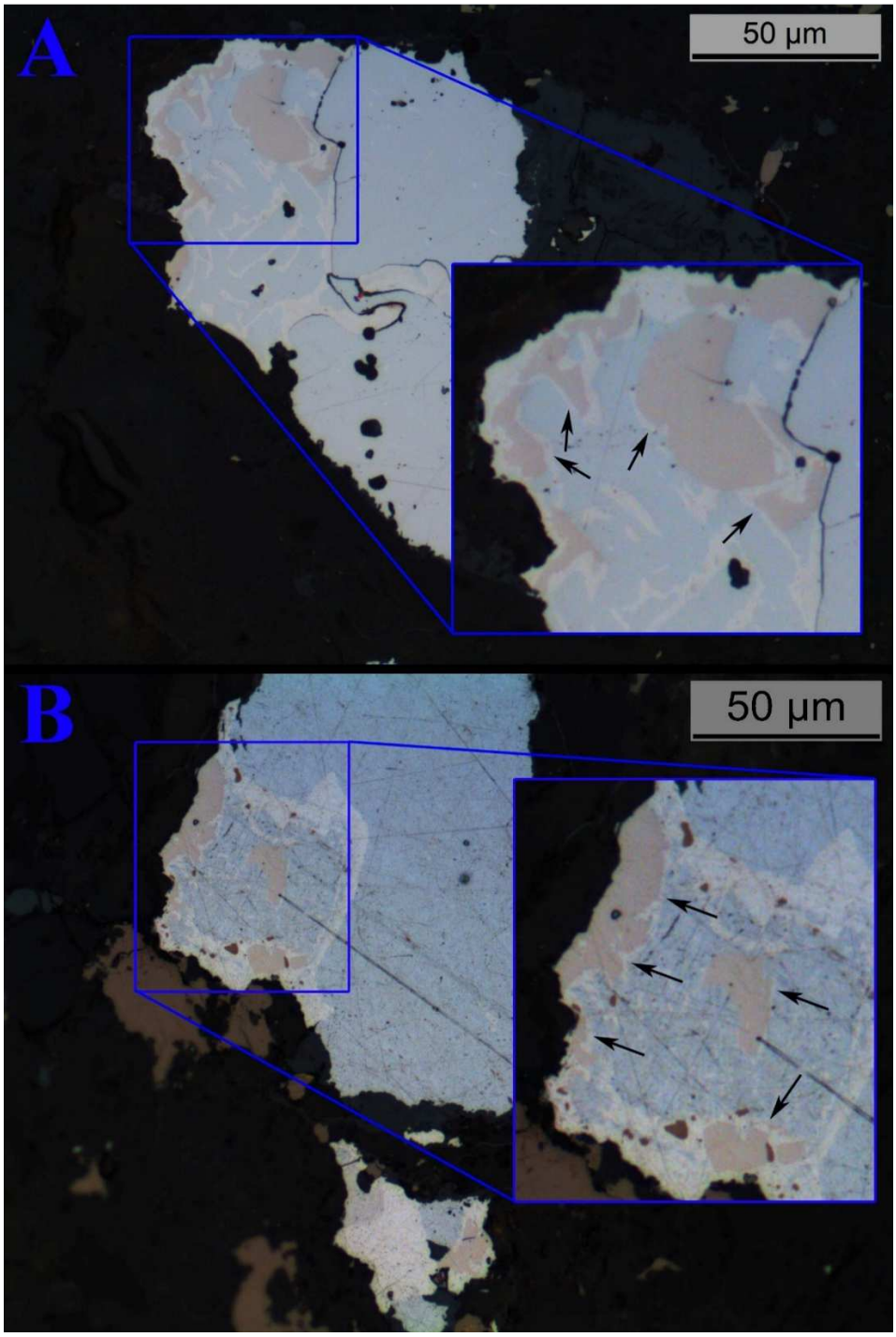

Figure 19. Photos A and B illustrate taenite (cream-colored) rimmed carbide (light tan) grains from NWA 10517 and NWA 10516. Photo A (0142-1-C-109) and B (0020-2-C-80) have the area of interest inset to more easily illustrate the rim on the carbide grains. Photo A also shows an interesting pattern to the carbide growth, where the carbide appears to curve around the kamacite (light blue). Reflected light image, color enhanced.

The textures that Tomkins (2009) described have been seen in several meteorites in this study, including NWA 10518, which is pictured in Figure 20 and Figure 21. The troilite inclusions are associated with carbide, as they share the same host metal. The carbide has also been noted in both figures.

An uncommon carbide texture that has been observed is the so called "budding" texture. It is characterized by multiple carbide grains projecting and seeming to nucleate from a taenite grain. Figure 22 gives two examples of this texture. In Figure 22a, the large metal grain has this budding texture surrounding every occurrence of taenite. The two insets give a larger view of the texture. In this texture, the carbides do not appear to "eat" into the taenite grain so much as grow off of it, given that the taenite is of relatively

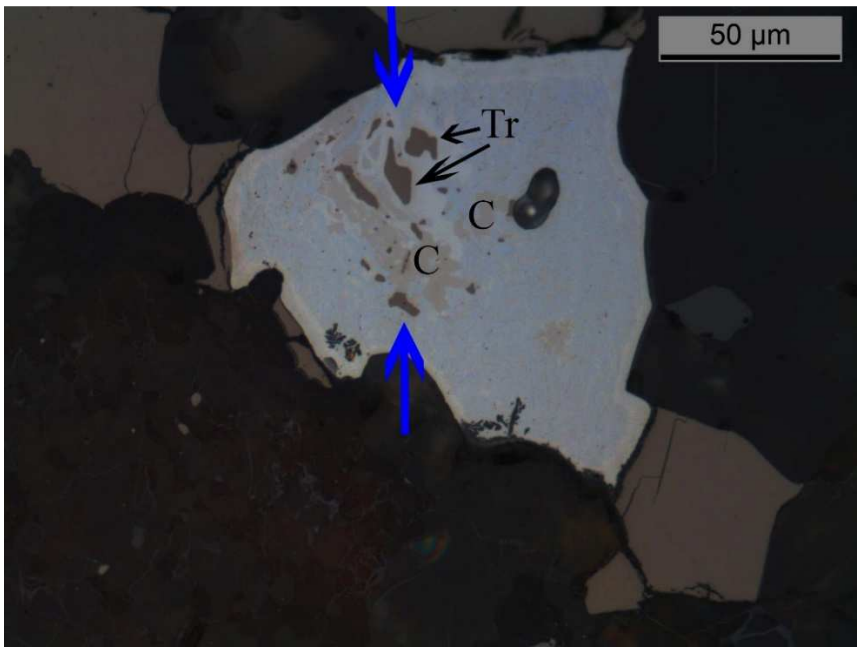

Figure 20. Troilite intergrowths in NWA 10518 (CML0157-2). Troilite (Tr) appears as globular, anhedral metal blebs inside of the host grain, blue arrows bracket the potential troilite trail. Complete troilite appears on the edges of the image as well as on the edges of the metal grain. C = carbide. Reflected light image 0157-2-C-218 has been color enhanced.

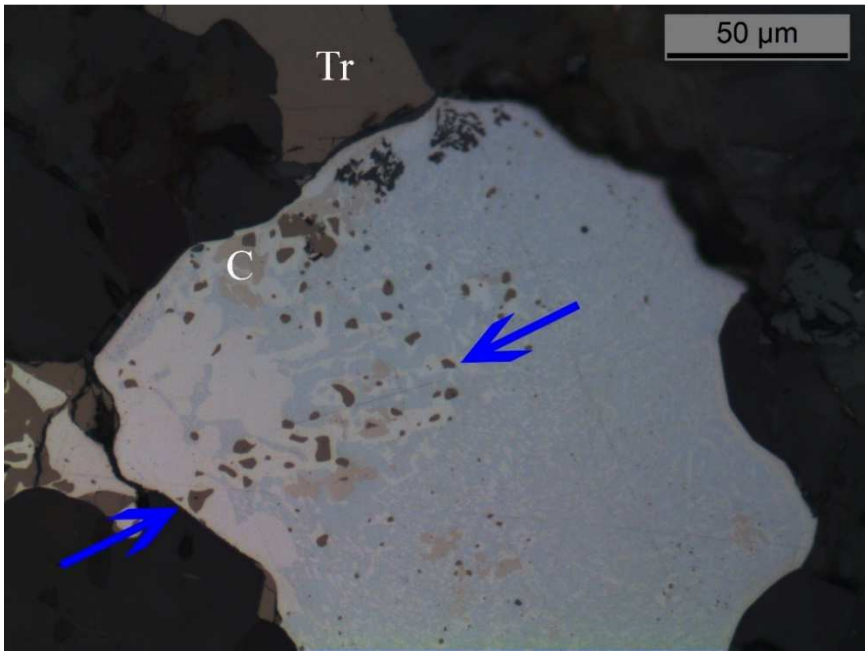

Figure 21. Additional troilite (Tr) intergrowths in NWA 10518 (CML0157-2). Troilite inclusions are small metal blebs scattered around the inside of the host metal. Blue arrows bracket the troilite trail. C = carbide. Reflected light image 0157-2-C-220 has been color enhanced.

uniform width. Figure 22a also has silicate inclusions scattered around the inside of the host metal. Most commonly, silicate minerals are observed to occur separate from the metals, not as inclusions. Figure 22b is another example of the budding texture that occurs in the same meteorite. This texture was primarily observed in Buck Mountain Wash, in the low type lithology.

Extreme anhedral textures for carbide that could represent intergrown grains were documented in all meteorites in this study. The complex intergrowths can be seen in Figure 23 and Figure 24. Figure 23 has the carbide forming adjacent to taenite laths and long parallel stretches of carbide can be seen in several places. Small islands of taenite exist inside the mass of carbide. Figure 24 is a complex intermixture that features a variety of textures. There are budding textures (area 1), taenite rims (area 2), and

subhedral textures along with the main anhedral mass. This type of anhedral texture is more rare than any other textures but is also more striking in their unorthodox appearance.

For an assemblage to be a CMA, it must feature a close spatial relationship between magnetite and carbide. For the purposes of this paper, a CMA is defined as an assemblage of metal grains that contains both carbide and magnetite, with both touching or in extremely close proximity such that it is likely they are touching in another cut of the thin section. This is seen below in Figure 25 and Figure 26. Figure 27 and Figure 28, by this definition are not CMAs because although magnetite is in the image, it is not in sufficiently close proximity to the carbide.

Several CMAs have been identified in the meteorites involved in this study, such as in Figure 25 and Figure 26 from NWA 10518 (CML 0157) where magnetite was identified either in contact with carbide or occupying the same metal grain as the carbide. However, the layered textures described by Krot et al (1997) do not occur in the meteorites in this study. Figure 25 is the closest example of the CMA Krot et al (1997) describe, but it differs in that the carbide occurs in one kamacite grain rather than as individual grains in the CMA or as a single grain attached to another metal grain. Krot et al (1997) also described their carbides as being irregularly shaped inclusions or as intergrowths with taenite while many of the carbides in Figure 25 are subhedral. Unlike those observed by Krot et al. (1997), carbide rims are not found as the outer layer around the CMAs in this study. Carbides in this study primarily occur in single metal grains

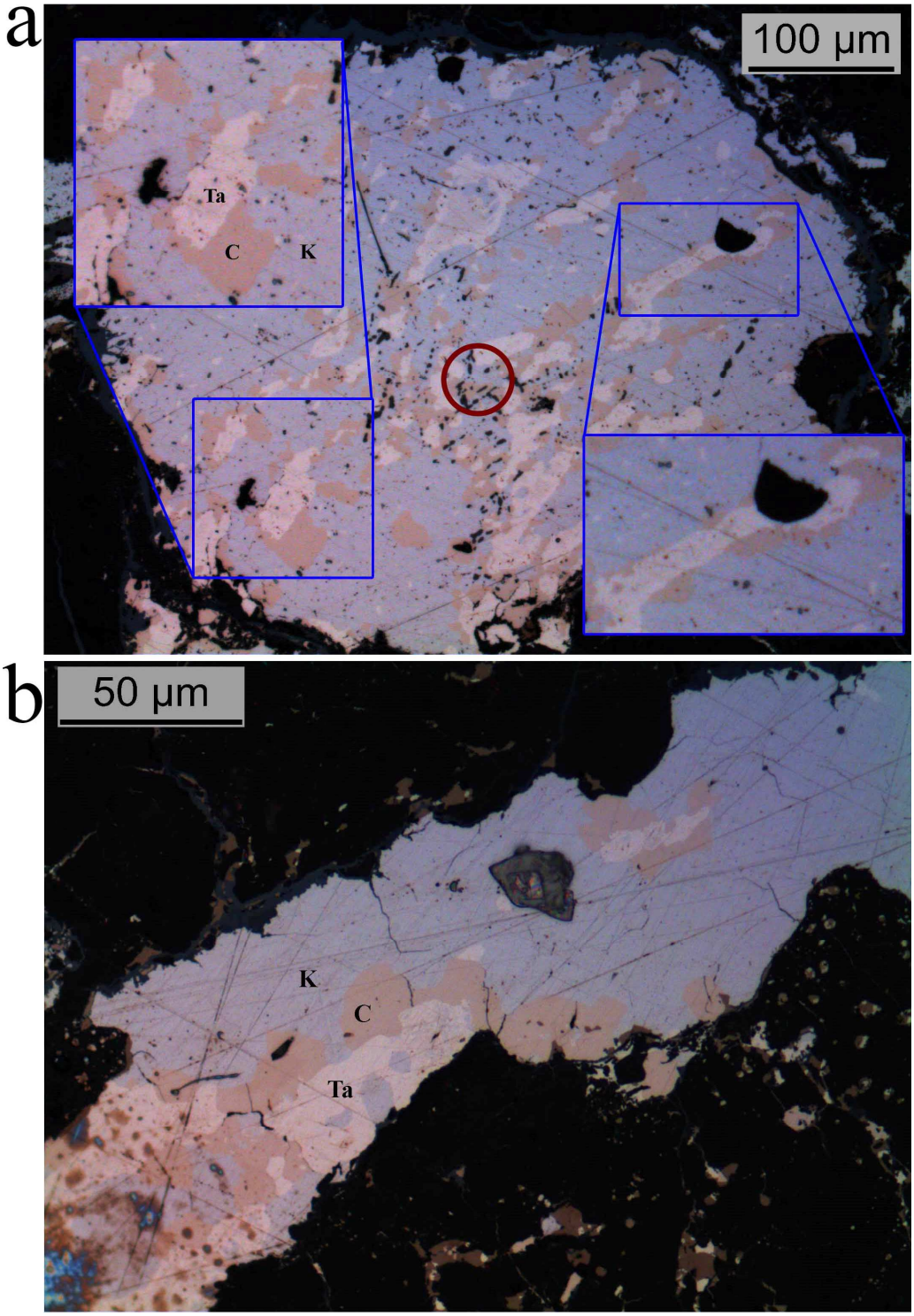

Figure 22. Budding texture from Buck Mountain Wash. A is image 0144-2B-C-120 and B is image 0144-2B-C-118. C = carbide, Ta = taenite, K = kamacite. The red circle in (a) refers to silicate inclusions present in the metal. Reflected light images, color enhanced.

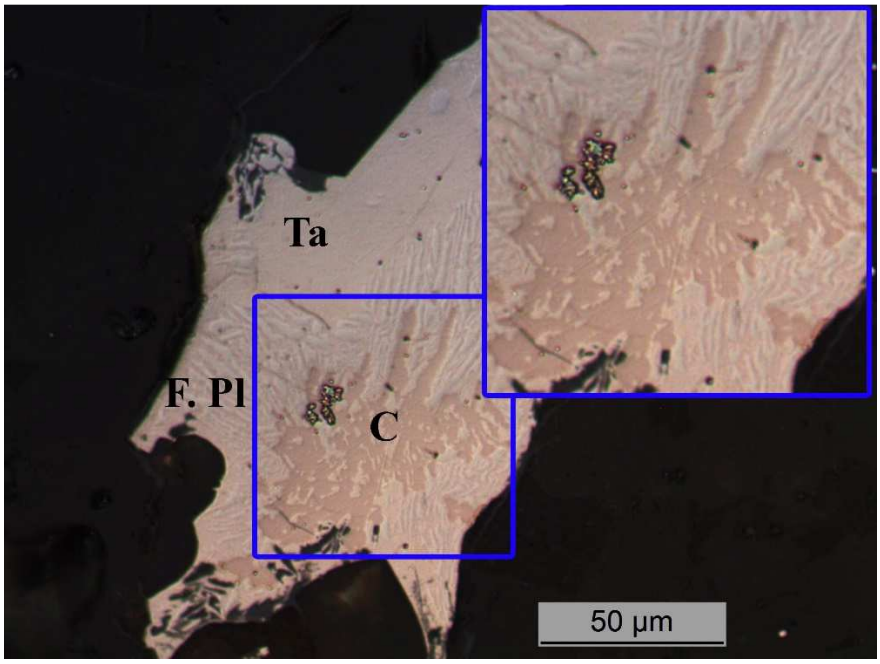

Figure 23. Anhedral formation of carbide NWA 10454 (CML0139-2). The fine-grained plessite is denoted by F. Pl, taenite with Ta and carbide with C. Reflected light image 0139-2-Carbide-80, color enhanced.

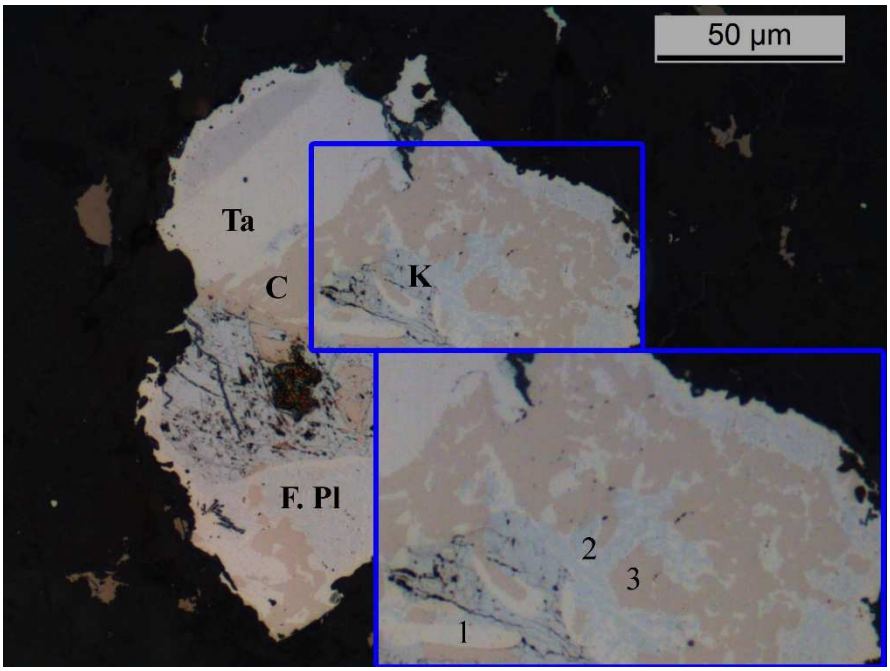

Figure 24. Complex, anhedral formation of carbide in NWA 10518(CML0157-2). Taenite = Ta, kamacite = K, fine plessite = F. Pl, and carbide = C. Several areas of interest have been numbered, a miner budding texture can be seen at 1, taenite rims at 2, and subhedral textures at 3. Reflected light image 0157-2-C-470 has been color enhanced.

rather than as a layered assemblage of various metal phases, which is the texture primarily seen by Krot et al (1997).

Table 5 examines the distribution of magnetite grains with respect to carbide. Three classifications were assigned, including 1) the presence of magnetite in the image with no contact with carbide or the host grain, 2) the presence of magnetite in the host grain of carbide but not in direct contact, and 3) the presence of magnetite in direct contact with carbide. The last category is what this study refers to as a "CMA". Finally,

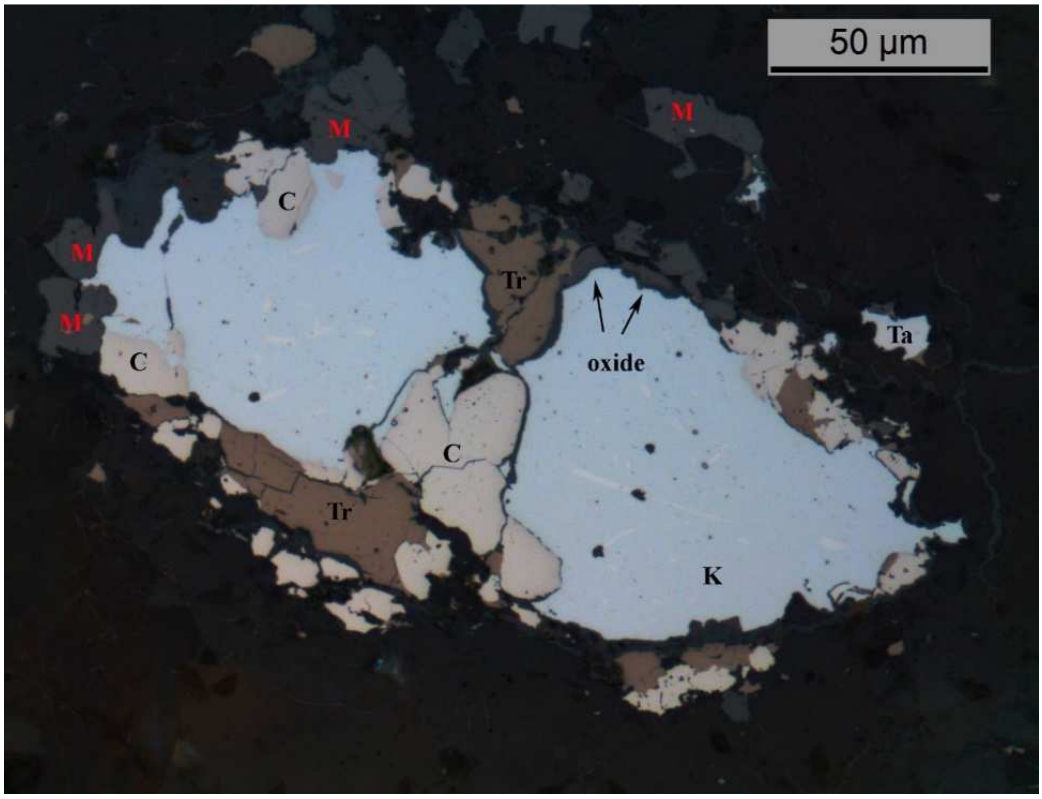

Figure 25. Example of a carbide-magnetite assemblage in NWA 10518. Several grains have been marked with their identifying corresponding letter. Carbide = C, magnetite = M, troilite = Tr, taenite =Ta, kamacite = K, and other oxide grains marked with arrows. Reflected like image of 0157-2-C-185, color enhanced.

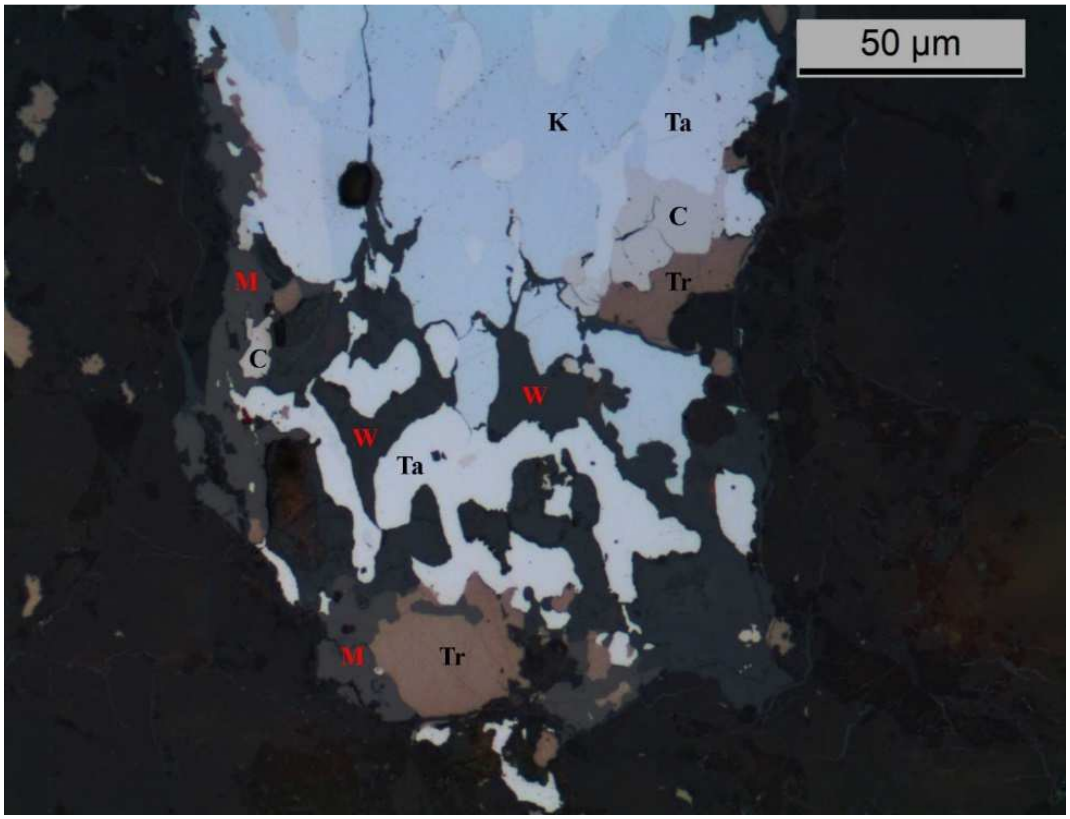

Figure 26. Illustrates a CMA example where carbide is in contact with magnetite and also distinct from magnetite, from NWA 10518. Carbide = C, magnetite = M, troilite = Tr, taenite =Ta, kamacite = K, and weathering product (iron hydroxide) = W. Reflected light image has been color enhanced and was given the designation 0157-2-C-109.

the percentage of CMAs for the whole meteorite thin section was determined and this is reported in the last column of Table 5. In two meteorites, the presence of CMAs is greater than ten percent of the total carbide grains while in the other instances they are no more than 4.5 percent of the total. The occurrence of magnetite not in direct association with carbide was much more frequent than the CMAs while the majority of carbide grains have no association with magnetite in any of the three categories.

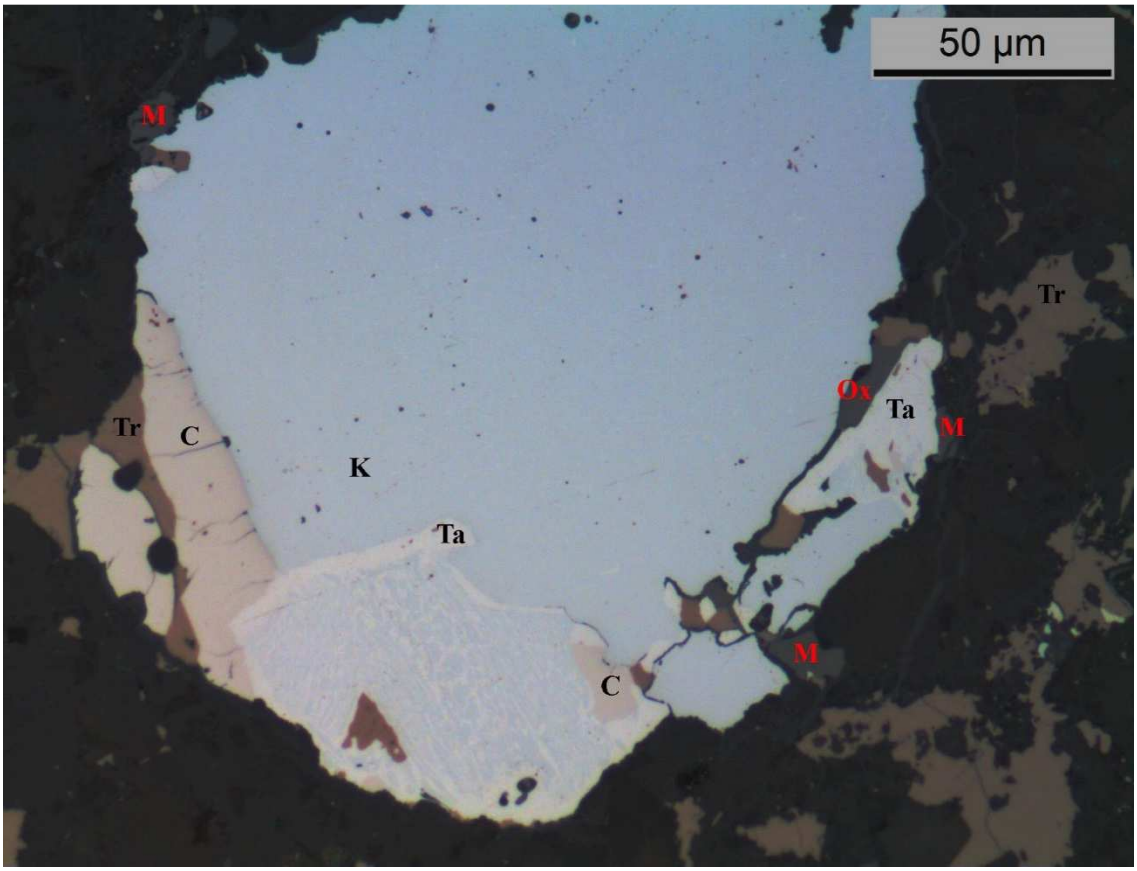

Figure 27. Carbide and magnetite share the same grain but where the magnetite is not in contact with carbide, from NWA 10518. Carbide = C, magnetite = M, troilite = Tr, taenite =Ta, kamacite = K, and other oxide or hydroxide = Ox. Reflected light image 0157-2-C-284, color enhanced.

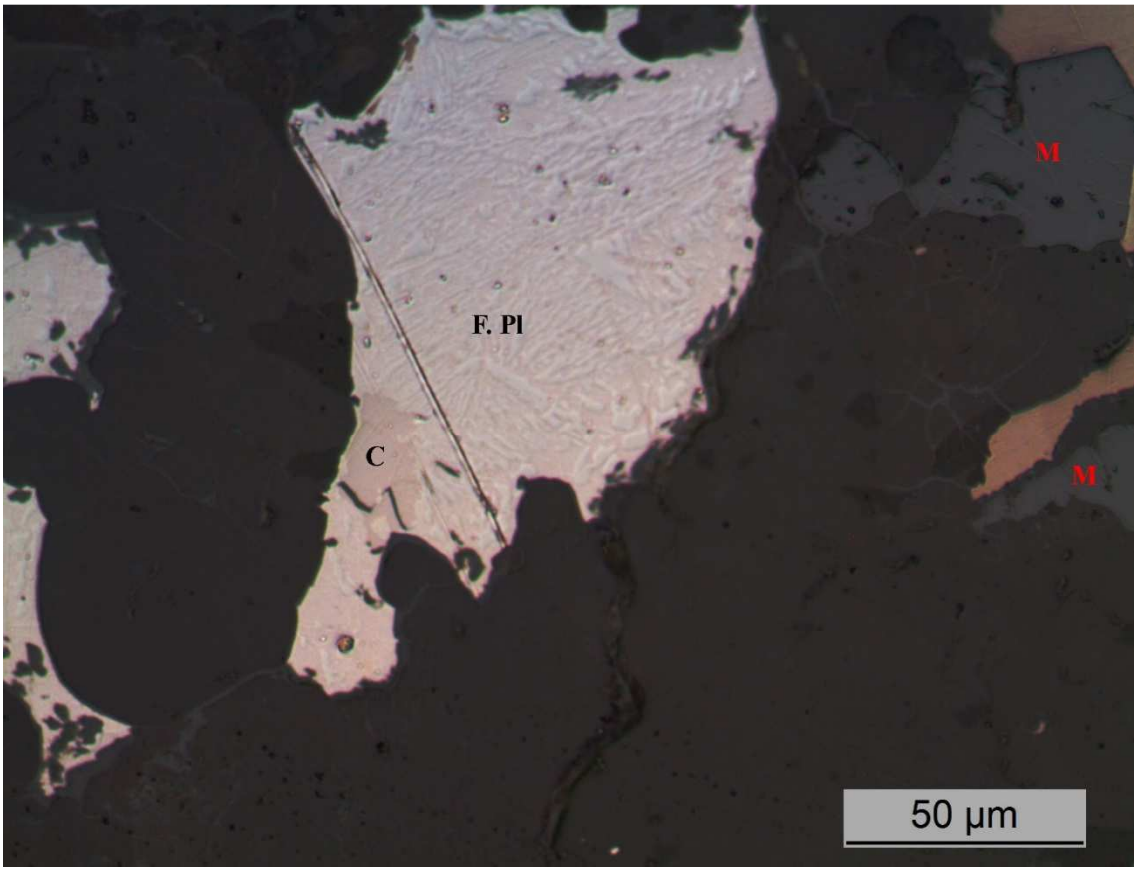

Figure 28. Example from NWA 10454 where magnetite exists separately from carbide and host metal grain. Most frequent occurrence of magnetite is like this. Designation 0139-2-Carbide-52. Photo color enhanced. This picture was also seen in Figure 14.

Table 5. Summary of the presence of magnetite and its relationship to carbide

Meteorite	Magnetite in image	Magnetite in grain with carbide (not in direct contact)	Magnetite in contact with carbide ("CMA")	"CMA" % of total carbide grains
NWA 10516	36	11	6	3.8
NWA 10518	211	14	25	4.4
Buck Mountain Wash	38	6	21	16.9
San Juan de Allende	6	1	0	0
NWA 10454	14	6	0	0
NWA 10517	42	13	5	2.4
NWA 11121	34	3	18	11.8

Compositions

To calculate the compositions of the carbide minerals, a correction procedure had to be applied. This procedure was discussed in detail in the methods section of this paper. Figure 29 shows the results of the correction procedure. Figure 29a includes the background carbon from the carbon coat across all metal phases. The results of the correction procedure can be seen in Figure 29b. The carbon in kamacite has been zeroed out. Many of the taenites also had their carbon content reset to zero, however a number of the taenite grains still display positive carbon values. With the exception of one value, there is a gap in the taenite values, between zero and approximately 0.3. This gap could be a threshold for the correction procedure in taenite and values above that threshold could represent non-zero carbon values in taenite.

The compositions of the carbides were explored by plotting the apparent corrected carbon values in weight percent against the nickel weight percent of the iron and nickel, Figure 30a. Two populations became apparent, at 1.75 and 5 wt% on the x-axis. The data populations have a spread to them, mainly in the C content, but within each spread there are groupings. These groupings are averaged and replotted with the standard deviations in Figure 30b, with the outliers left as the gray symbols. Furthermore, the carbon values for four carbides were added as lines for compositional comparison.

Carbide group A plots close to the cohenite line in Figure 30b, and carbide B is close to the haxonite line. Carbide C does not correlate with a known carbide. The averaged weight percent values for the three carbide groups in Figure 30b can be found in Table 6. Hutson et al., (2016) provided the data for the cohenite and haxonite columns,

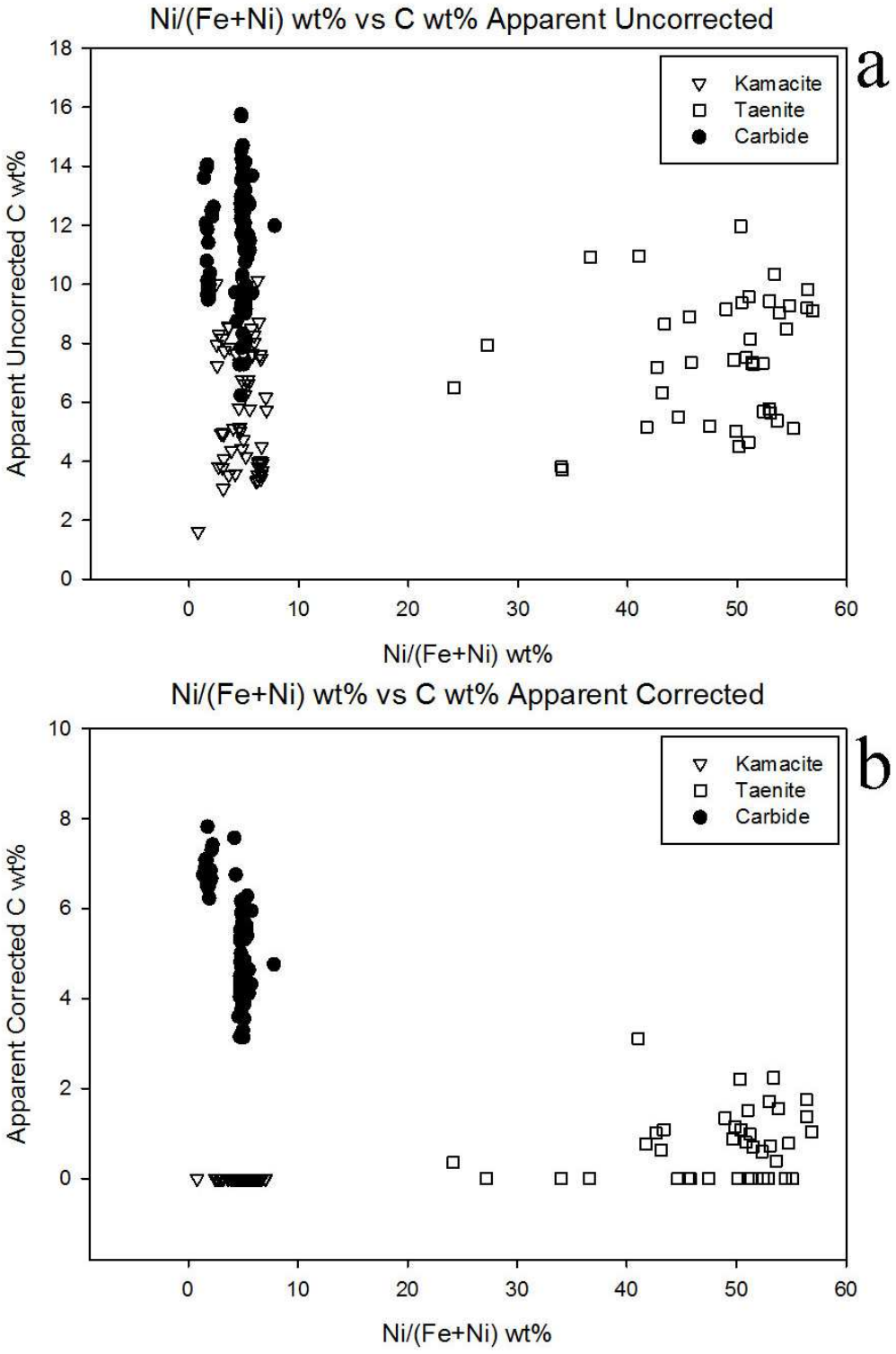

Figure 29.The results of the correction procedure can be seen above. The top graph (a) shows the data before the correction was applied and b is the data after the correction was applied.

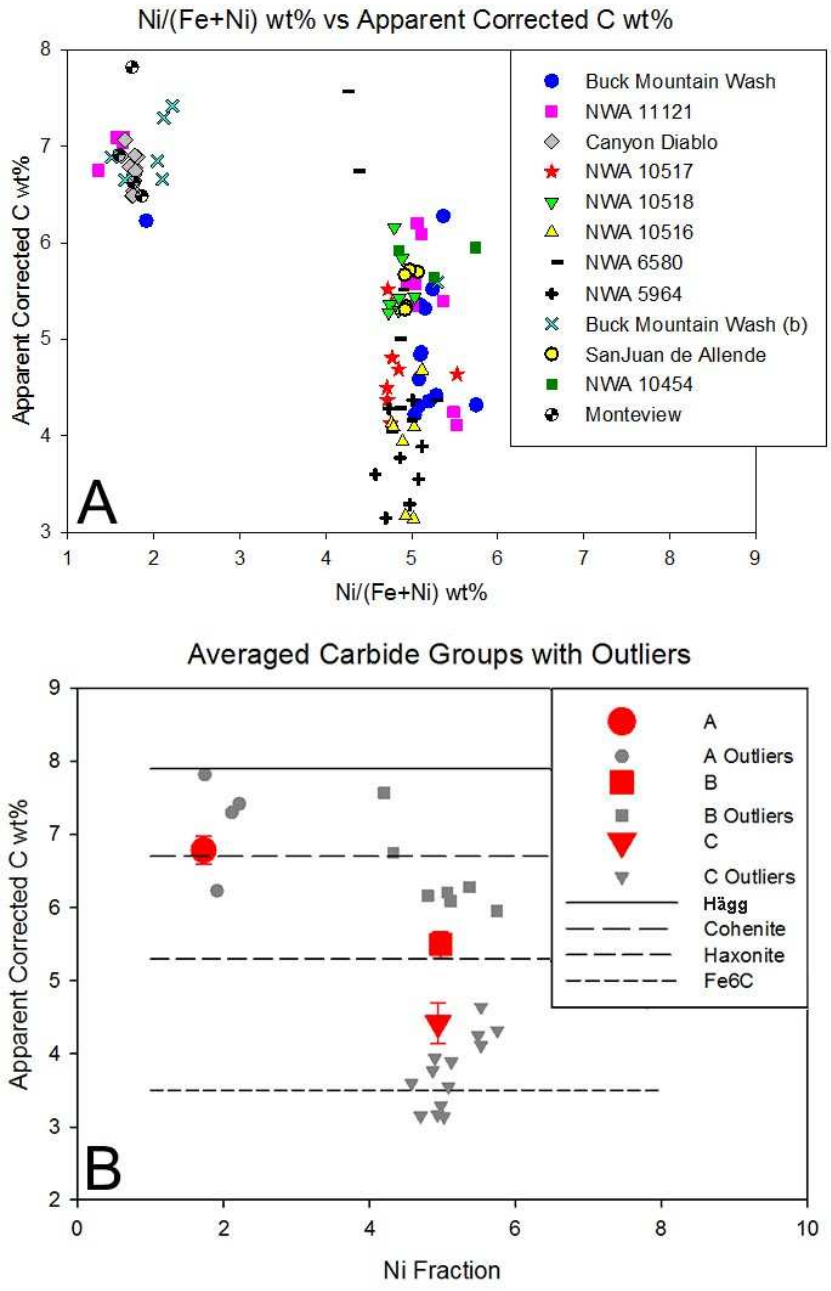

Figure 30. A: the nickel weight percent against the apparent corrected carbon weight percent. Two distinct populations are seen, at 1.75 and 5 on the x-axis. These are further explored in B, in which clumps are averaged and outliers left out. Four carbides were plotted as lines based on their carbon weight percent as comparison. Other carbides are known to exist but not relevant for this study. Averages and standard deviations can be found in Table 6. One data point is covered by the legend and excluded from calculations.

which was collected through an EMP study with no correction procedure for the data. Standard deviations are shown in parentheses to the side of each value. The carbon values of Hutson et al. (2016) differ somewhat from the data collected during this study and to the carbon lines seen in Figure 30b. In regards to this study, uncertainties include assuming an even carbon coat and that there was no carbon present in kamacite. Additionally, Hutson et al. (2016) used cobalt (Co) as the element for plotting and carbide identification while carbon was used in this study. Therefore, the data for this study is approximate in comparison and normalized to 100. However, the carbon values obtained by Hutson et al, (2016) differ also from the stoichiometric carbon values seen in Figure 30b. Cohenite has a carbon weight percent value of 6.7 and haxonite 5.3. Carbide group A has been tentatively identified as cohenite based on the average carbon value of 6.8 wt%, which is close to the ideal 6.7. Carbide group B has an average value of 5.5 wt% C and has been given the designation of haxonite.

The correction procedure applied for this study yielded group A and group B, which are close approximations to two carbides, cohenite and haxonite. The nickel and iron contents for the

Table 6. Inferred composition of carbides using correction technique (normalized to 100 for A, B, and C) with standard deviations

	A	B	C	Cohenite*	Haxonite*
Fe wt%	91.6 (0.2)	89.8 (0.3)	90.9 (0.3)	91.2 (0.6)	89.7 (0.7)
Ni wt%	1.6 (0.1)	4.7 (0.2)	4.9 (0.2)	1.7 (0.1)	4.5 (0.2)
C wt%	6.8 (0.2)	5.5 (0.2)	4.4 (0.3)	4.7 (0.2)	4.8 (1.0)
n	23	30	23	6	100

* Data courtesy of Hutson et al., 2016

corresponding haxonite and cohenite groups are similar in this study and that of Hutson et al. (2016), which also separate both groups on the x-axis on the plots in Figure 30 and in the Co vs Ni plots in Hutson et al, (2016). While the carbon values vary between the datasets, the populations plot similarly and likely represent the same minerals. Apparent differences in C contents mostly could stem from the different correction procedures used.

Carbide group C does not have a C content of a known carbide phase and instead plots in between haxonite and Fe_6C. This could represent submicroscopic mixtures of different types of carbide grains, which could result in a blended composition. Alternatively, a hypothetical carbide with the formula Fe_5C would have a carbon weight percent of 4.1, which would closely correspond with the group C carbide. However such a carbide has not been found to exist. Alternatively, experimental error was large enough to effect carbide group C and throw the value off of ideal and those grains are either haxonite or Fe_6C.

Interestingly, the cohenite was only found in the H chondrites, Buck Mountain Wash and NWA 11121 and the iron meteorites Monteview and Canyon Diablo. However, both Buck Mountain Wash and NWA 11121 also have haxonite present, as shown in Figure 30a. The carbides that plot at 5 wt% Ni are more abundant than the cohenite group at approximately 2 wt% Ni . Sampling more carbide grains could yield a larger population of cohenite grains, but currently they were found only in H chondrites.

Cooling Rates and Closure Temperatures

Two meteorite samples were investigated for in-depth cooling rate analysis, NWA 11121 and NWA 10518. Three types of Ni zoning patterns were 1) the regular "M" profile of taenite, 2) a reheated profile (flat interior), and 3) asymmetric profile where the center was not the lowest nickel content. Figure 33 illustrates all three profiles. For the reheated profiles, the radius was equated to the distance across which Ni is zoned upward sharply to the highest nickel rim, as a measure of the diffusion distance during cooling following a reheating event that homogenized the core. Asymmetric profiles had their radius determined by measuring from the lowest nickel content to the highest nickel content rim. A possible bias affecting the data would be a sectioning bias based on where the linescan was taken. This was minimized by taking care to align the linescan across the center of the taenite grain as much as possible.

These three profiles are plotted separately on metallographic cooling plots in Figure 31 and Figure 32 as circles, down triangles, and x's corresponding to regular, reheated, and asymmetrically zoned grains, respectively. Figure 31 illustrates the results obtained from NWA 11121 and Figure 11 shows the thin section with the marked clasts. The high-type (HT) clasts show a distinct, slower cooling rate than either the low-type (LT) clasts or the carbide bearing host material, this is seen in the red symbols in graph A. The reheated and asymmetrical symbols (down triangles and x's) show a systematic offset to the left from the regular taenite profiles, which could be indicative of a resetting or reheating event. The carbide bearing host grains plot with the low-type (LT) clasts, however they also show a wider distribution along the x-axis but still indicate faster

cooling than the high-type (HT) material. The reheated carbide bearing host grains in the lower right of graph B are significantly shifted down and to the right at relatively fast cooling rates, which can be explained by rapid cooling following a reheating event that homogenized the central Ni content of the taenites.

Figure 32 demonstrates the cooling environments for NWA 10518 and the lithologies and clasts can be seen in Figure 12.. The carbide bearing host material seems to indicate the presence of diverse cooling environment in the amount of scatter among the points. For the carbide bearing host material, the reheated profiles differ from the regular profiles. This could be due to the small grains that allowed diffusion across the entire grain, giving a complete profile rather than a reheated, or asymmetrical profile for the larger taenite grains. The presence of shock melt in NWA 10518 means that locally reheated grains could have been reset more than grains farther from shock melt. These reheating events imply that faster cooling rates represent cooling under later reheating events while the slower cooling rates are older events.

It should be noted that NWA 10518 (L3-6) and NWA 11121 (H3-6) represent different parent bodies, indicated by the L and H in the classification (Burbine et al., 2002). The way in which brecciation and heating occurred on these two bodies may have differed, with evidence for slower cooling preserved more in the H chondrite.

Additionally, from the taenite linescans, the estimated temperature formation range for carbide minerals was determined using a digitized version of the Fe-Ni phase diagram from Willis and Goldstein (1981). The core and rim nickel values of the taenite linescans record different temperatures. The core of the taenite grain records the

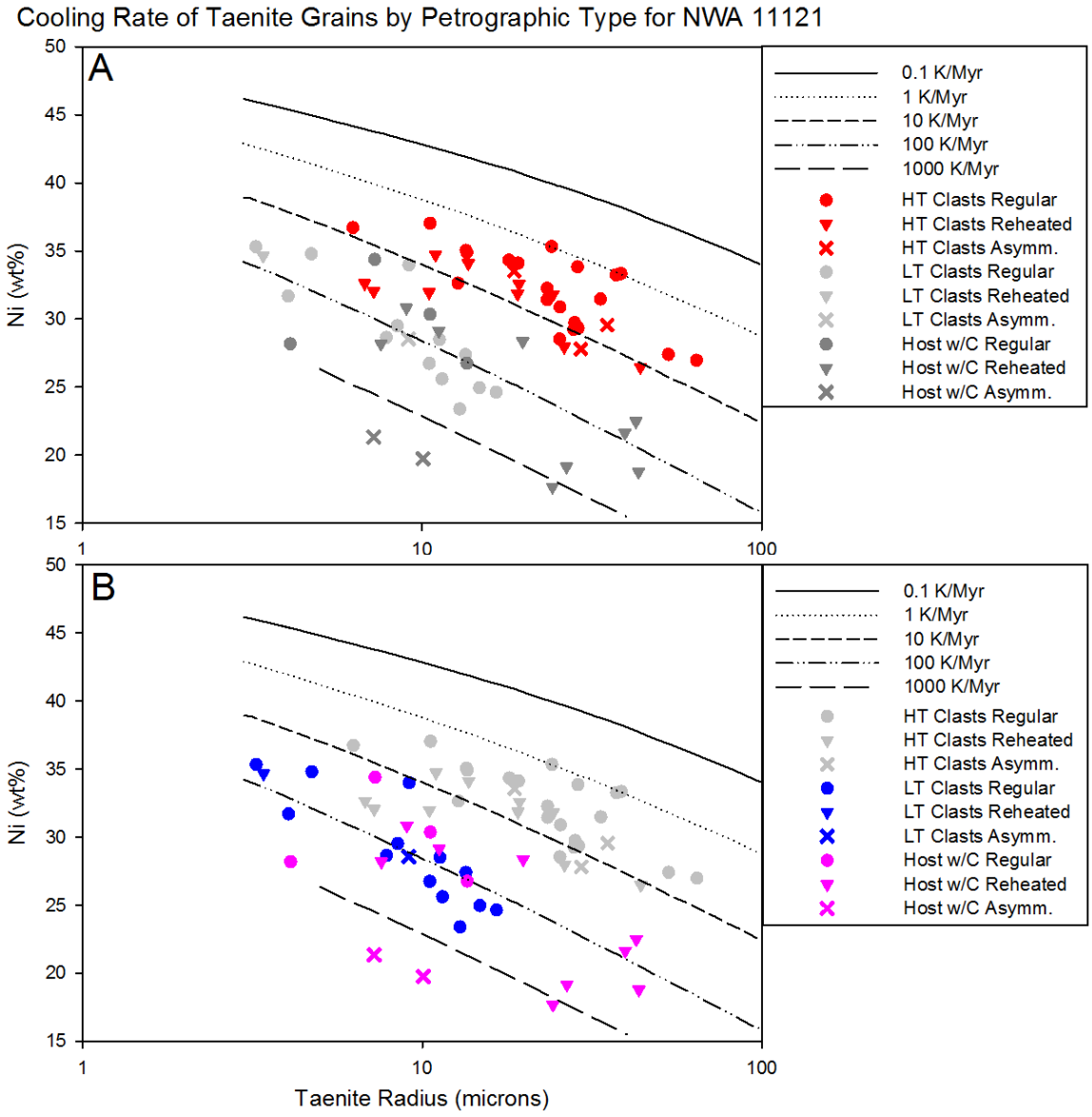

Figure 31. Cooling rates from taenite grains in NWA 11121 (CML 0172), separated by clasts, and carbide bearing host grains. HT stands for high-type clasts, and LT for low-type clasts.

temperature at the start of cooling while the rims capture the closure temperatures of the taenite grains (Wood, 1967). Figure 31 and Figure 32 were created using only the core nickel values, to determine the cooling rate. Table 7, which is based on Schepker (2014), has the average temperatures of both the core and rim of the taenite grains, as well as the

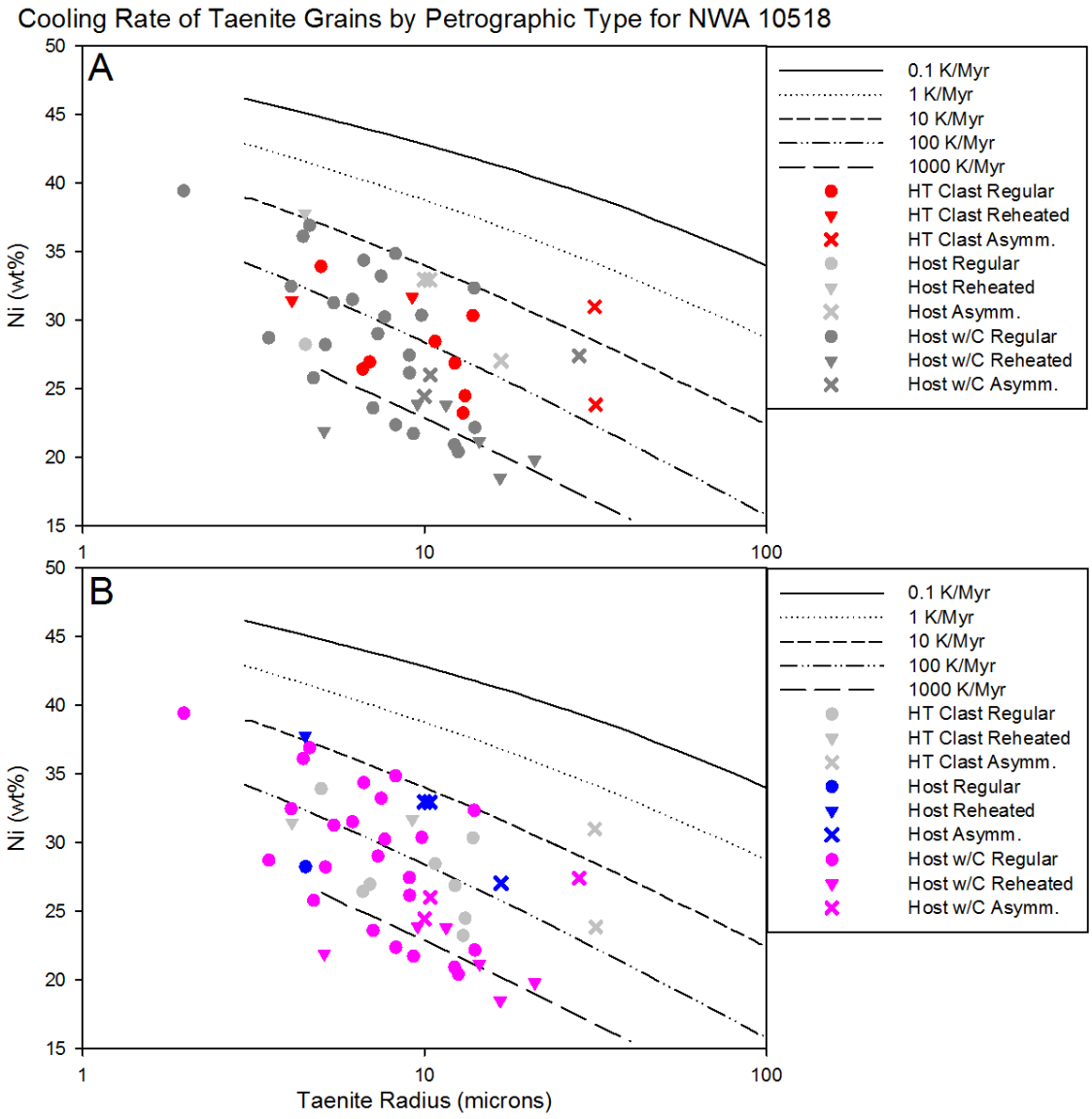

Figure 32. Cooling rates from taenite grains in NWA 10518 (CML 0157), separated by clast, host, and carbide presence. HT stands for high-type clasts, and LT for low-type clasts.

standard deviation, minimum and maximum for the three lithologies in NWA 10518 and NWA 11121. Both meteorites record similar temperature ranges for the core and the rim. No lithology is substantially different from the others, given the standard deviations. The digitized phase diagram created by Schepker (2014) matched closely with the published

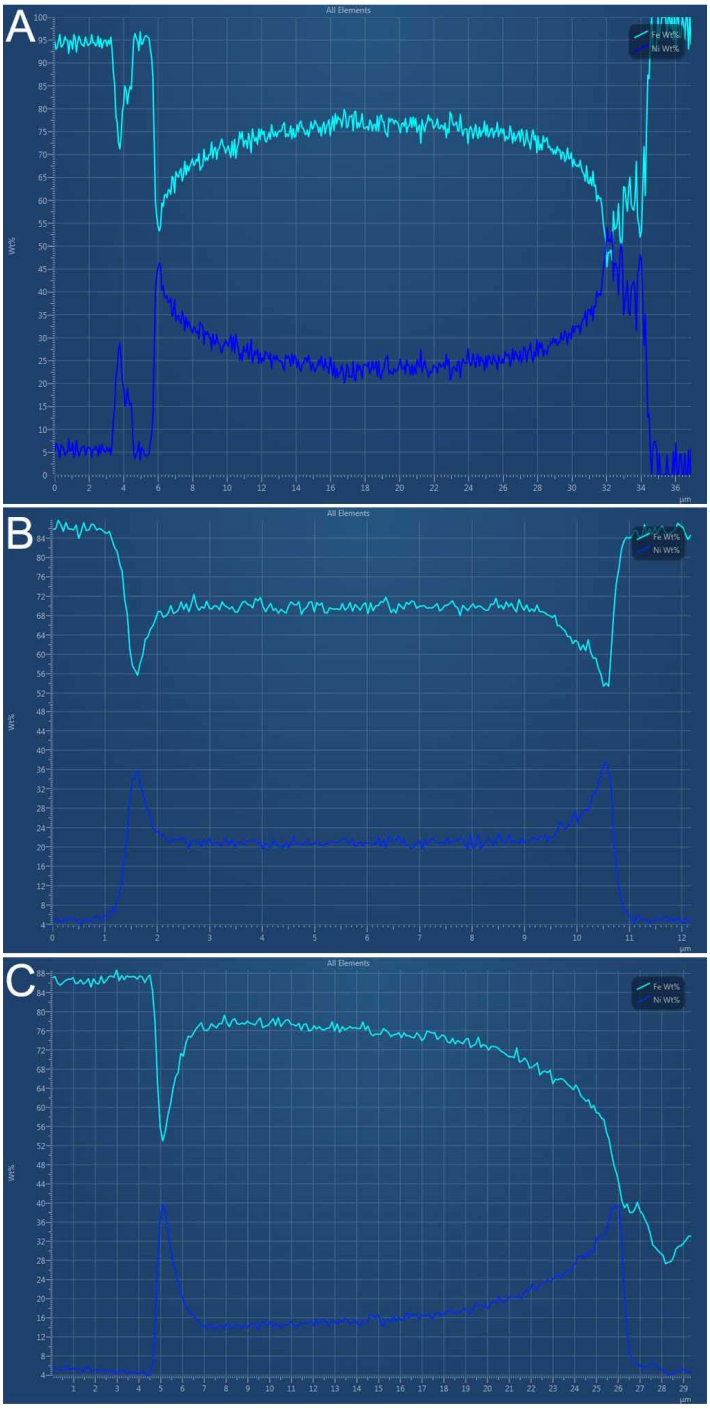

Figure 33. The three types of taenite profiles observed. In all three profiles, the cyan line is iron and the blue line is nickel. A: the classic "M" profile of a taenite grain, collected from NWA 10518, Line Data 13. B: The flat interior (reheated) taenite profile, from Buck Mountain Wash, Line Data 8. C: The asymmetric taenite profile, from NWA 11121, Line Data 1.

Fe/Ni phase diagram from Scorzelli (2008). The mismatch implied an estimated accuracy within 10°C, and so two significant figures were used to report the data in Table 7.

Table 7. Temperatures (°C) from core and rim values in taenite associated with carbide to estimate carbide formation range

NWA 10518		Average	St Dev	Minimum	Max	Count
HT Clast	Core	630	40	560	690	12
	Rim	380	30	330	410	
Host	Core	580	60	500	650	5
	Rim	370	30	340	400	
Host w/C	Core	640	70	470	750	33
	Rim	380	50	300	570	
NWA 11121						
HT Clasts	Core	580	40	510	660	34
	Rim	390	60	340	560	
LT Clasts	Core	620	50	540	690	15
	Rim	430	40	360	490	
Host w/C	Core	670	60	550	750	15
	Rim	370	40	320	410	

Romig and Goldstein (1978) provided the experimental data for the formation of cohenite in Fe-Ni-C systems. The system begins with taenite that then decomposes into kamacite and cohenite. Four isotherms were examined by Romig and Goldstein (1978); 730°C, 650°C, 600°C, and 500°C. Carbide does not begin to coexist with kamacite and taenite until the temperature has cooled to 650°C and then is present through the 600°C and 500°C isotherms (Romig and Goldstein, 1978).

Okamoto (1992) created a phase diagram for the Fe-C system, Figure 34, for the steel making process. The phase diagram covers a larger range of temperatures and more clearly illustrates the temperature stability of carbide, which is less than 727°C for low C contents. This temperature is implied by the coexistence of kamacite, taenite, and carbide

in the carbide-bearing meteorites in this study, and according to the Fe-C phase diagram, this can only occur at 727° and below. Both the Fe-C and Fe-Ni-C isotherm phase diagrams suggest an upper limit of formation temperature of ~650-730 °C for the carbide-bearing metal particles. Ferrite and austenite are the terrestrial equivalents of kamacite and taenite. As the temperature decreases, carbide forms with kamacite at the expense of taenite over a wide range of bulk compositions. Taenite can hold small amounts of carbon, which is eventually decomposes into carbon free kamacite and carbon rich carbide. It should be noted that the phase diagram in Figure 34 is metastable and is a nickel free system. Additionally, the phase diagrams treat all carbide as cohenite and at least two carbide phases has been identified in this thesis. However, it does provide solid idea on how the process could have taken place and the temperatures that the phases formed at.

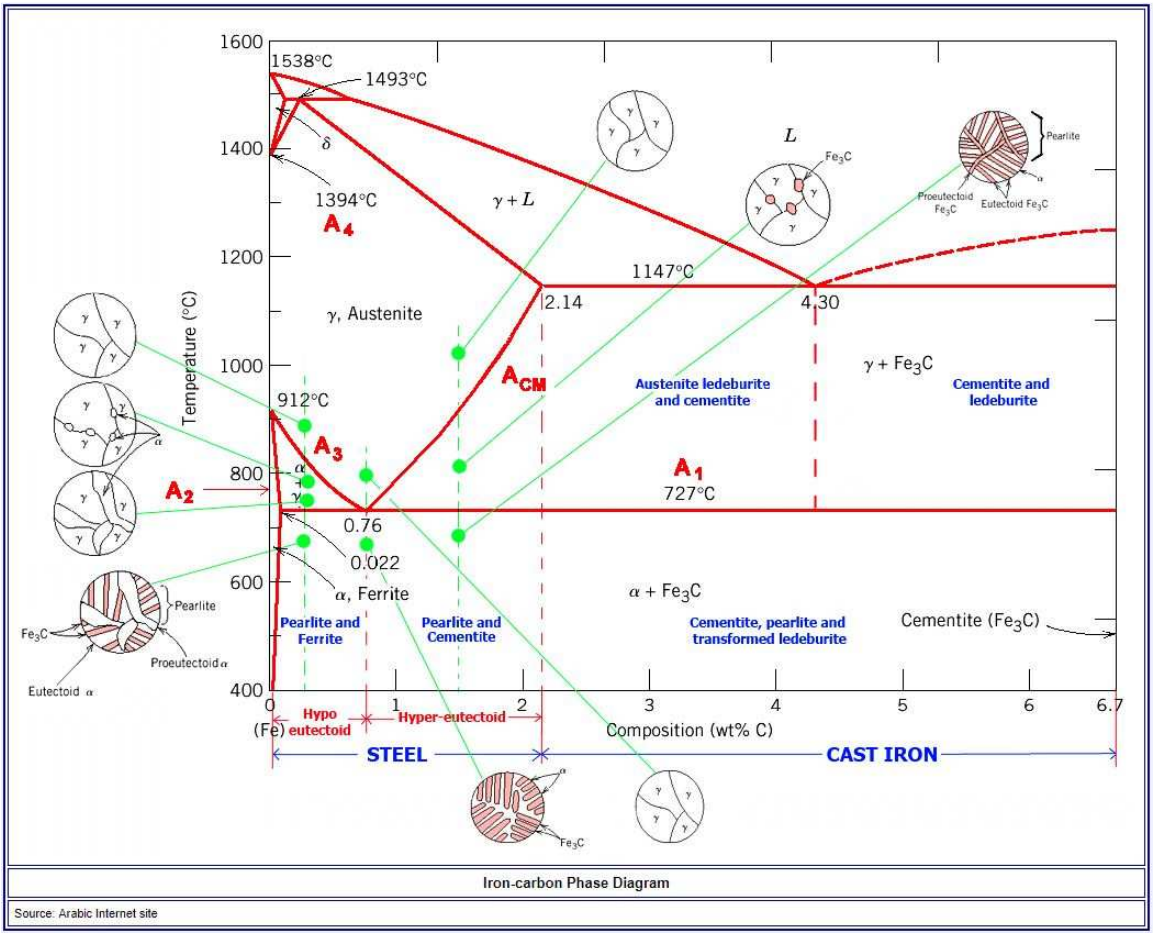

Figure 34. Phase diagram of the Fe-C system from Okamoto (1992). The terrestrial analog for kamacite is ferrite (alpha), taenite is austenite (gamma) and cohenite is cementite. Ledeburite and pearlite refer to texture types that contain carbide. As the temperature decreases, carbide forms with kamacite at the expense of taenite.

Discussion

Origin by aqueous alteration

Previous research by Krot et al. (1997) supported carbide formation through aqueous alteration of iron in metal-troilite nodules. The possible reaction sequence was discussed in the background section of this paper. However, other than the occasional presence of magnetite, no other evidence of aqueous alteration was found during the course of this study. Furthermore, it was noted that the textures of the CMAs found by Krot et al. (1997) differ significantly from this study, as mentioned in the Textures and Mineralogy portion.

Table 5 summarized the presence of magnetite and its relationship to carbide. While magnetite can be seen in the same field of view as carbide-bearing metal phases with some frequency, the CMAs are rarely seen. In San Juan de Allende and NWA 10454, no CMAs were found to occur. NWA 10516, 10517, and 10518 had CMA percentages that were less than 4.5%. Buck Mountain Wash and NWA 11121 were the only two meteorites that had higher CMA occurrences, at 21% and 18% respectively. CMAs do not regularly occur in conjunction with carbide and thus do not strongly support aqueous alteration.

Due to the textural differences observed between the images and descriptions provided by Krot et al (1997) and those seen in this study, it is possible that carbides have several possible methods of formation. The observations and images referenced by Krot et al (1997) may be indicative of formation through aqueous alteration while the carbides in this study argue for a different formation hypothesis, discussed in more detail below.

Additionally, the presence of magnetite alone is not enough to argue formation through aqueous alteration. No other hydrous minerals were found during microscopy. Bleached chondrules are another possible indicator of aqueous alteration, which are radial and cryptocrystalline chondrules that have a porous outer layer, visually distinguished by a "bleached" area, or light gray to white, in the chondrule (Grossman et al, 2000). These were not found to occur in the carbide-bearing meteorites. Based on this evidence, and that listed above, it is unlikely that the carbide minerals in this study formed through aqueous alteration.

If carbides formed through aqueous alteration, carbides would primarily form on the edges of grains, similar to bleached chondrules, rather than in the grain interior. Table 4 indicates the occurrence of carbide by location on the edge or inside of the host metal grain. While many of the carbides do occur on the edges of grains, up to a third of them occur on the inside of host grains. The occurrence of these carbides is not be easily explained by aqueous alteration and it is unlikely that they formed through aqueous alteration.

A final potential problem with the aqueous alteration hypothesis for carbides is that even CMAs may not have formed purely by aqueous alteration. Keller (1998) studied carbide particles in Semarkona and suggested that the carbides there formed during prograde metamorphism, distinct from a later, more oxidizing stage at lower temperatures that formed rims of magnetite. In this case, the association of magnetite with carbide would not indicate simply one process but rather two different processed occurring at different times.

Origin by thermal metamorphism

If carbides formed through thermal metamorphism, a correlation between petrographic type and the presence of carbide would be expected as type 3 chondrites are the least metamorphosed and type 6 the most. This would imply that type 6 material would contain more carbides. As Figure 7 demonstrates, there does not appear to be any such correlation. A complicated, inverse correlation is more likely as type 6 clasts in genomict breccias rarely contain carbide. If carbide is present in such clasts, it is in quantities far lower than that of surrounding materials, as seen in Figure 11, Figure 12, and Table 2. In non-brecciated meteorites, carbide was not found to occur in petrographic type 4, 5, or 6 meteorites and only a single type 3 meteorite was found to be carbide-bearing. All other carbide-bearing meteorites in this study are genomict breccias, which contain a mixture of petrographic material, with type 3 always present. Thermal metamorphism cannot explain the occurrence of carbide observed.

Origin by shock heating

The third formation scenario is through shock heating. There is some support for this hypothesis. Shock melt is present either in thin section or hand sample for all the carbide-bearing meteorites. Furthermore, troilite injection zones have been found associated with carbide in every carbide-bearing meteorite. They are not common, as troilite must border the metal grain for them to form. The troilite injections imply that the surrounding troilite reached a high enough temperature to potentially form minor melts that were then injected into the nearby metal grains (Tomkins, 2009). Hauver and Ruzicka (2011) reported the bulk carbon composition of NWA 5964 to be from ~0.1 to

1.6 weight percent. When compared to phase diagrams created by Tomkins et al., (2013) regarding iron carbides, this places an upper limit of 1350°C for melt temperatures. However, the textures surrounding the troilite injections are distinct from those produced by the partial melting of the metal, troilite minerals, and the silicates. The troilite grains that surround the metal that hosts the injections do not show evidence of melting and mobilization (Figure 6). Additionally, no shock melt surrounding the affected grains was observed and zoned taenite was preserved near the troilite injected metals. This implies that short term, high spikes of temperature occurred to liberate the sulfur from troilite and diffuse it into the metal while still remaining subsolidus and leaving the surrounding silicate material primarily unaffected (Tomkins, 2009). Additionally, as the troilite did not separate out, they must have experienced fast cooling.

However, if carbides were formed through shock heating, a correlation between the presence of carbide and shock stage would be expected. This was not observed, Figure 8. The distribution of the carbide-bearing meteorites by shock stage almost displays a bell curve distribution. Carbide was also never found to occur in the melt zones of meteorites. Further, carbide appears to be destroyed or prevented from forming in shock-blackened areas, which show evidence for melting of metal and troilite. For example, Figure 5 provides a good illustration of this in that the shock melt contains no carbide grains and the shock blackened area, which experienced enough heat to melt and mobilize the troilite, see Figure 6, and likely destroyed or prevented the formation of the carbide minerals that are present in the melted and shock blackened portions of the thin section. Four carbides were found in the shock blackened area, two near the boundary

where the rest of the carbide-bearing host material is and two in the largest metal grain in that area. The large size of the metal grain likely insulated the carbides and allowed them to survive the heating event. Table 2 has the breakdown of carbide location by lithology. The shock melt does not contain carbide, shock blackened areas have very few carbides that survive, and high type clasts do not have as many carbides and the mixed lithologies of the host material or the lower type clasts.

The relationship between shock heating and the presence of carbide is a complicated one. It appears that too much heating can destroy or prevent the carbide from forming, as it is never found in melt and sometimes not in heavily shock area, Figure 5. However, carbide can be associated with the troilite injections, which are formed through shock, and shock melt is present in all carbide-bearing meteorites.

Impact and Brecciation History

Carbide minerals require a source of carbon and thus might be related to the amount of C present in the chondrites (Jarosewich, 1990). Carbon content in L, LL, and H meteorites decreases slightly from L to H, as seen in Figure 35. The transition from Type 3 to Type 4 meteorites shows the largest decrease in carbon content and Types 4-6 show slight differences. H meteorites have a smaller carbon content than the Ls or LLs, and so there might be less frequency of carbide found in H chondrites due to less carbon. Genomict breccias could have more carbon than a strict type 4, 5, or 6 chondrites. The carbon content of the meteorites in this study is an unknown, but the proportion of type 3 material could be used as a proxy for likely C content, and there might be differences in the amount of carbide minerals in different chondrite groups that reflect the average

content of C in H vs. L and LL chondrites. The carbide bearing chondrites in this study have type 3 material present. The carbon necessary to form the carbides could originate in the type 3 material or in other organic material or other mineral phases. It should be pointed out that although having sufficient bulk C is probably necessary to create carbides, it is not a sufficient condition. Three out of four type 3 and presumably C-rich ordinary chondrites were not observed to contain any carbide. Something besides bulk C content appears to be critical in enabling carbides to form.

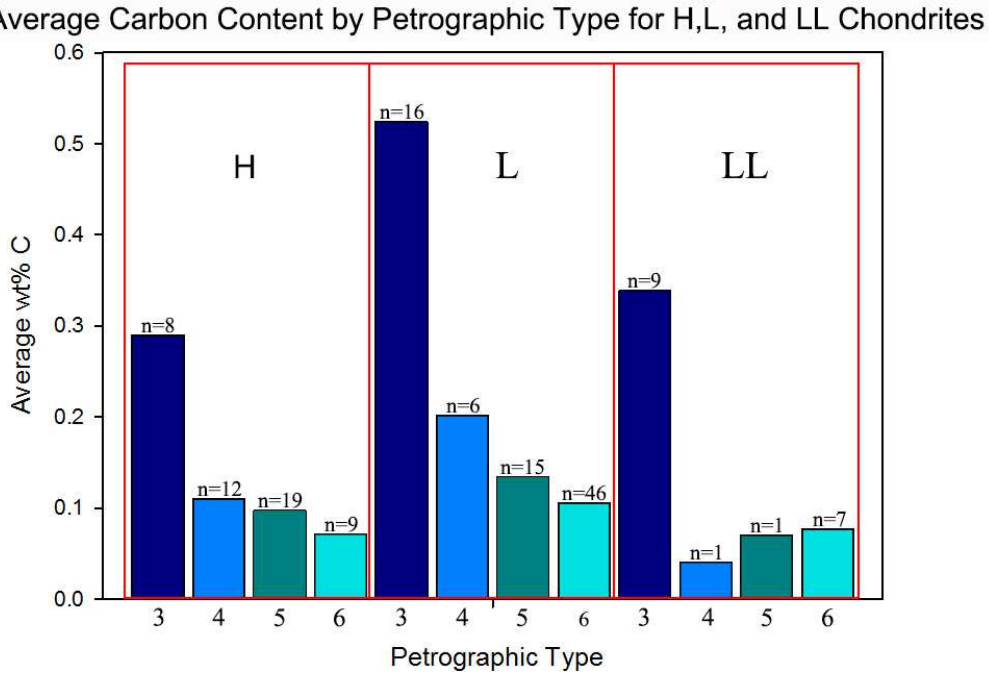

Figure 35. Average carbon contents of ordinary chondrites by class and petrographic type. Number of values used in each average indicated at the top of the column. Carbon values collected from Jarosewich, 1990.

With one exception, the chondrites that contain carbide are genomict breccias (Figure 7, Table 1, and Table 2) that contain a mixture of petrographic material from 3 to 6. It is widely accepted that the different petrographic types formed in different cooling environments. The onion-shell model is frequently cited as the way ordinary chondrites

formed. The model has the higher petrographic types forming deep within an asteroid body, where they cool slowly, and the lower petrographic types closer to the surface where they cool more quickly and preserve their unequilibrated material (Dodd, 1969). It should also be noted that others have suggested parent body disruption and then reintegration into loose rubble piles (Scott and Rajan, 1981). Figure 36 is an illustration of both models from Scott and Rajan. (1981). For the purpose of this paper, the onion-shell model is primarily assumed. In this model, type 6 material forms deep within the parent body and is then impact excavated, causing the type 6 material to mix with the shallow, cooler material and forming carbide.

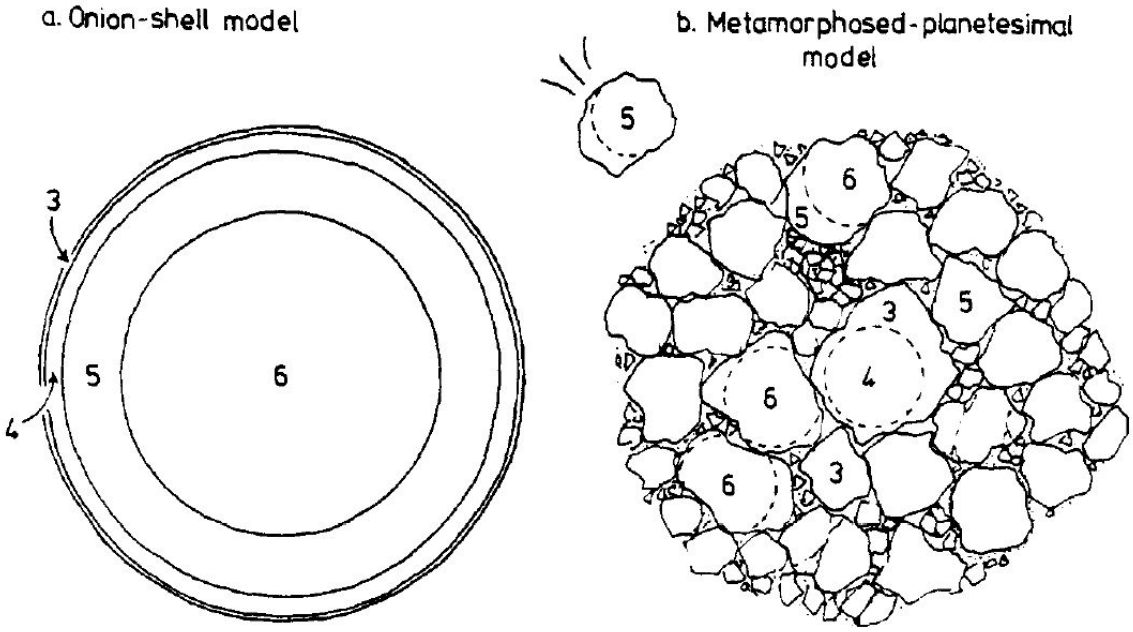

Figure 36. Two formation models after Scott and Rajan (1981). A shows the classic onion-shell model where the higher type materials form deeper in the parent body with the lower type material located progressively outward. B, which is also known as the rubble pile model, shows the disrupted and reintegrated model where smaller bodies cooled complete before accreting into a parent body.

The cooling rates represented for NWA 10518 in Figure 32 illustrate a wide scatter and overlap between the high type clast and the host material, which implies that the two lithologies were mixed together and then cooled. The cooling rates could have varied based on proximity to the heat source, either by depth if the bodies were hotter towards to center or towards impact melt deposits if the bodies were primarily heated by impact events. The carbide minerals that occurred in taenites sampled for cooling rate data and the taenite not associated with carbide had a range of cooling rates that are similar to other grains, therefore the carbide could have formed under a range of cooling temperatures after the mixing, or approximately 10-1000 K/Ma. This means that the carbide wasn't extremely sensitive to exact formation settings. Additionally, since the scatter in cooling rates for the grains sampled had to be maintained, late brecciation likely happened after initial cooling so that the grains from different location could be reassembled under mostly cool conditions and not reset their cooling rate.

The wide scatter of cooling rates is also present for NWA 11121 in Figure 31, however the high type clast displays a markedly different cooling pattern than the low type clast and host material. The host material is a mixture of low and high type, which means that a mixing event must have taken place. The cooling rate of carbide falls into the 10-1000 K/Ma range, but the slower cooling range is only inhabited by the higher type clast material. This indicates that the formation of carbide most likely happened after the scrambling of material to make a breccia, under a range of temperature conditions, but before the high type clasts were incorporated into the meteorite as the differences in cooling rate had to have been preserved. This also implies late brecciation. Both

meteorites have a cooling rate of about 10-1000 K/Ma for the carbide, after the incorporation of the carbon rich type 3 material. The reheated taenite grains in both figures imply that there was some heat after brecciation, but it was not prevalent as many grains were not affected.

Two heat sources are possible for the formation of carbide, radiogenic heating and impact heating. Radiogenic heating is consistent with the large volumes of parent material experiencing metamorphism, like the onion-shell model would indicate (Bennett and McSween, 1996). This would allow the mixing of the hotter type 6 material with the cooler and carbon enriched type 3 material to form carbide. This would also be consistent with the lack of correlation between the presence of carbide and shock stage. Additionally, regarding formation through impact heating, shock melting destroys the carbide in any directly affected area. However, the heat from nearby impact melt could be enough to cause the formation of carbide.

Carbide is not stable at high temperatures, as indicated in the phase diagram in Figure 34, nor is it stable when in contact with liquid at low carbon concentrations. It is only at high carbon contents at the eutectic that carbide can exist in contact with liquid and perhaps as a liquid itself. Through phase diagrams (Goldstein and Romig, 1978, Okamoto 1992, Figure 34) and the work of Fang et al. (2010), and the textural observations of the carbide minerals, it is known that austenite (taenite) formed first and has the most carrying capacity for carbon. Kamacite will carry little to no carbon. As cooling took place, carbide became a metastable phase as the carbon from austenite was formed into a carbide mineral. Fang et al. (2010) also determined that the crystal structure

of austenite (taenite) and haxonite (carbide) are extremely similar, which would make it more likely for the austenite (taenite) to decompose into carbide.

The textures in Figure 18 and Figure 19 illustrate the taenite rims that can be found on carbide grains, an observation also seen by Fang et al. (2010), which supports the idea that the carbide minerals nucleate within taenite rather than kamacite. The carbides then grow at the expense of taenite, but in the case of the taenite-rimmed structures, did not completely replace all of the taenite. The additional textures seen in Figure 22, Figure 23, and Figure 24 further support this idea. In Figure 22, carbide can clearly be seen budding off of taenite grains that exist within a larger kamacite. Figure 23, and Figure 24 are complex intergrowths of carbide where the carbide appears as extreme anhedral forms.

Evidence for carbides forming through shock wave propagation and associated with heating and disruption can be seen in the association of carbide with troilite inclusions, Figure 20 and Figure 21. Tomkins (2009) argued that the shock wave from impact events caused irregular heating, which released sulfur from troilite and injected it into other metal phases, leaving an injection trail that could be followed from the outer edge of the metal grain to inside, indicated by the blue arrows in Figure 20 and Figure 21. Carbon could be liberated from C -enriched material in a similar manner to sulfur and follow the same migration pattern into the host metal as the sulfur did, forming carbide grains. In Figure 20 and Figure 21, the carbide is found mixed with troilite in the same migration paths. As Tomkins (2009) argued, formation through shock wave propagation would explain the irregular occurrence of the inclusions within thin sections and

meteorite classes. It would also allow enough heat to free the sulfur and carbon but not melt the other preexisting minerals. This would also indicate that carbides can form through smaller heating events and not at higher temperatures.

Formation Temperatures

The best evidence for the formation temperatures of carbides are the closure temperatures estimated from coexisting taenite, which indicate they formed at ~370-670 °C (Table 7). This supports the evidence above that higher temperatures (above 670°C) may have mostly led to carbide destruction or prevention rather than growth.

This temperature range is also consistent with the spatial association of carbide with type-3 material (Figure 7). Type 3 material is evidence that carbides did not form at high temperatures, as the high temperatures would have equilibrated the type 3 material. And type 3 material is present in all the carbide-bearing meteorites, summarized in Figure 7. According to Huss et al. (2006), petrographic type 3 ordinary chondrites experienced a range of temperatures from approximately 200°C to 600°C. Type 3 ordinary chondrites are subdivided into further subtypes and the temperature range given above is a very broad estimate to encompass all type 3 chondrites. For example, Semarkona is a LL3.00 meteorite that was given an upper limit of approximately 260°C, much lower than for other ordinary chondrites (Huss et al., 2006). Buck Mountain Wash was examined by Hutson et al., (2007), who determined that the Lithology B had a classification of H3.4-3.5 while Lithology A is a type 3-6 mixture (Hutson et al., 2013). Based on the temperatures of subtypes summarized by Huss et al. (2006), a subtype of 3.4-3.5 could correspond to ~350-600 °C. Further research has given various estimates for the type 3

subtypes that fall within the 200°C to 600°C range with most approximations giving the temperature range 350°C to 600°C (Huss et al, 2006, Hutchison, 2004), although Scott et al. (2014) determined that type 3 H chondrites reached peak temperatures of 600-675°C.

The temperatures for aqueous alteration would have been lower. For low type (3.00-3.15) ordinary chondrites, the temperatures experienced through aqueous alteration would have been below 260°C, and <300 °C and possibly <100 °C for carbonaceous chondrites (Brearley, 2006). These aqueous alteration temperatures are considerably lower than needed to form the carbides of this study and support the conclusion that they did not form by aqueous alteration.

Although the temperatures calculated for carbides in this study are higher than expected for aqueous alteration, they are not as high as expected for peak thermal metamorphism, which produced temperatures up to 800-900 °C (Huss et al., 2006). Therefore, whether carbide formed by radiogenic or impact heating, the heat source could not have been powerful as too much heat would destroy or prevent carbide formation and destroy the type 3 material they are associated with.

Closure Temperatures and Plessite

In Romig and Goldstein (1978), phase diagrams isotherms are presented at 730°C, 650°C, 600°C, and 500°C. The carbide cohenite does not appear on the phase diagram with both kamacite and taenite until 650°C and below. When applying the bulk compositions in Hauver and Ruzicka (2011) for carbon and nickel in cohenite to the isotherms of Romig and Goldstein (1978), the carbides fall into the three-phase triangle region containing carbide + kamacite + taenite at 650°C or 600°C. The three phases

cannot form together at the 730°C isotherm according to the phase diagrams, especially at low carbon values. Taenite and carbide can form at the 730°C isotherm at high nickel and carbon values as the taenite begins to decompose into carbide and kamacite (Romig and Goldstein, 1978).

Romig and Goldstein (1978) found that cohenite nucleated at taenite/kamacite interfaces and previous taenite grain boundaries. The cohenite always nucleated out of the taenite rather than kamacite (Romig and Goldstein, 1978). This is consistent with the observation made during this study as carbides were found either on the edge of metal grains or at grain interfaces, Table 4.

Additionally, many of the carbides were found in plessitic or blocky intermixtures of kamacite and taenite, Table 3 and Figure 15. The formation of plessite is controlled by the parent taenite's nickel content before it decomposes sequentially into several possible phases, which include martensite, kamacite, and tetrataenite. The temperature range that plessite forms at is from ~600°C to 200°C (Goldstein et al., 2006). This process results in plessitic textures that contain many more interface boundaries that carbide nucleation could take advantage of and a temperature range similar to what carbide is expected to form at.

Identification of Carbide

The carbide minerals can be identified with relative ease using the SEM, when the correction method is applied. In Figure 30a and b, the carbide minerals plotted in three main clusters. Group A matched well with cohenite and Group B with haxonite. Group C falls in between two carbide lines, haxonite and Fe_6C, and compared to Groups A and B,

has the widest scatter in C contents. Group C data points likely represent a sampling of two or more different carbide grains with an averaged composition as the result. A fine-scale intermixture of two carbides, cohenite (Fe_3C) and Haag (Fe_5C_2) was described for Semarkona as revealed by TEM studies (Keller, 1998). This intermixture was also observed by Hutson et al., (2016) from EMP data. More carbide grains would need to be sampled to determine the third carbide. Tentatively, based on the scatter for Group C, it could be the Fe_6C carbide mineral, however, only a small number of data points were plotted around that composition line.

In any case, the correction method created and applied for this study is capable of distinguishing between haxonite and cohenite, with the possibility of a third carbide, using SEM data. The chemical formulas calculated from the averaged groups closely match that of the carbide minerals haxonite and cohenite.

Conclusions

There is little support for the idea that the carbides of this study formed by aqueous alteration, as has been previously suggested for ordinary chondrites. Carbide association with magnetite is minimal with most of the carbide bearing meteorites in this study having less than 5% of the carbides occurring in CMAs. Two meteorites were at 18 and 21% CMA occurrence and no other evidence for aqueous alteration was found. The textures of the carbides described by Krot et al. (1997), like the layered assemblages, were not seen to occur. The formation temperatures, cooling rates, and closure temperatures all provide temperatures that are too high to have been from aqueous alteration. For the carbides in this study, it does not seem like aqueous alteration was the formation method.

Whether shock heating alone could have been responsible for creating carbides, such as previously suggested, is more equivocal. There is no correlation between shock stage and carbide occurrence. Carbide was never found in shock melt, but each carbide-bearing meteorite had shock melt present. Shock blackened areas are less likely to contain carbide with proximity to melt. It appears that too much heat will destroy the carbide minerals or prevent them from forming. Meteorites that contained carbide also contained type 3 material. There is an anti-correlation between petrographic type and presence of carbide. High type clasts have little to no carbide, and the carbide can be found with the type 3 material or in the mixed host lithology that also contains type 3 material.

Carbide can occur as anhedral, subhedral, and euhedral minerals. Carbides tend to be small, however several grains have been found to be up to several hundred microns across. Carbides primarily occur on the edges of the host metal, but roughly 25% occur on the inside of the metal. When they do occur inside, they are always in contact with a fracture or grain boundary. They have not been found occur without such contact with another interface. Carbides are commonly found in plessitic or blocky mixtures of kamacite and taenite due to the transformation of taenite into carbide and kamacite.

Carbides formed through an event that provided a weak heat source that left the type 3 material they are associated with intact. Two distinct cooling rate patterns were observed in NWA 11121 and NWA 10518 and the carbide cooling rates are similar to that of low type or mixed lithology host material, approximately 10-1000K/Myr. In NWA 11121, the high type clast had a distinctly slower cooling rate than the host or low type clast while in NWA 10518, the high type clast and host material had similar cooling rates.

The closure temperatures are comparable to those experienced by the type 3 material, ~300°C to ~600°C. Through the application of heat, carbon was liberated from type 3 material, taenite, or other carbon rich sources and nucleated out of the taenite. Remnant taenite rims and the budding texture are possible indications for this process. The heating event that formed carbides could not have been in excess of the temperatures experienced by type 3 material, otherwise the petrographic type 3 would be have been destroyed. Troilite injections that are associated with carbide also indicate a lower temperature for carbide formation, with an upper limit of 911°C and fast cooling.

Carbide minerals can be positively identified using the SEM, even with carbon coated thin sections. Furthermore, using the correction technique outline in this thesis, haxonite and cohenite can be further identified from the linescan data with accuracy along with the possibility of a third carbide.

References

Bennett, M.E.III, and McSween, H.Y. Jr., 1996, Shock features in iron-nickel metal and troilite of L-group ordinary chondrites: Meteorites & Planetary Science, v. 31, p. 255-264.

Bennett, M.E.III, and McSween, H.Y. Jr., 1996, Revised model calculations for the thermal histories of ordinary chondrite parent bodies: Meteorites & Planetary Science, v. 31, p. 783-792.

Bischoff, A., Scott, E. R., Metzler, K., and Goodrich, C. A., 2006, Nature and origins of meteoritic breccias: Meteorites and the early solar system II, p. 679-712.

Brearley, A.J. and Jones, R.H., 1998, Chondritic meteorites, in Papike, J.J., eds., Planetary Materials: Washington, DC, Mineralogical Society of America, p. 313-398.

Brearley, A.J., 2006, The Action of Water: Meteorites and the early solar system II, p587-624

Buchwald, V. F., 1975, Handbook of iron meteorites, their history, distribution, composition, and structure: Center for Meteorite Studies, Arizona State University.

Burbine, T.H., McCoy, T.J., Meibom, A., Gladman, B., and Keil, K., 2002, Meteoritic Parent Bodies: their Number and Identification: Asteroids III, University of Arizona Press: Tucson, p. 653-667.

Dodd, R.T., 1969, Metamorphism of the ordinary chondrites: A review: Geochimica et Cosmochimica Acta, vol. 33, p. 161-203.

Fang, C.M., van Huis, M.A., Sluiter, M.H.F., Zandbergen, H.W., 2010, Stability, structure and electronic properties of γ-$Fe_{23}C_6$ from first-principles theory: Acta Materialia 58, p. 2968-2977.

Fredriksson K., Jarosewich E., and Wlotzka F, 1989, Study Butte: A chaotic chondrite breccia with normal H-group chemistry: Z. Naturforsch, v. 44a, p. 945-962.

Goldstein, J.I. and Michael, J.R., 2006, The formation of plessite in meteoritic metal: Meteoritics & Planetary Science 41, Nr. 4, p. 553-570.

Grokhovsky, V.I., Brusnitsyna, E.V., and Yakovlev, G.A., 2015, Haxonite in Chelyabinksh LL5 meteorite: 78th Annual Meeting of the Meteoritical Society: abstract #5272.

Grossman, J.N. and Brearley, A.J., 2005, The onset of metamorphism in ordinary and carbonaceous chondrites: Meteoritics & Planetary Scient 40, Nr. 1, p. 87-122.

Grossman, J.N., Alexander, C.M. O'D., Wang, J., Brearley, A.J., 2000, Bleached chondrules: Evidence for widespread aqueous processes on the parent asteroids of ordinary chondrites: Meteoritics & Planetary Science #35, p. 467-486.

Harries, D., and Langenhorst, F., 2014, Haxonite from 25143 Itokawa and its implication for metamorphic parent body fluids: 77th Annual Meteoritical Society Meeting, abstract #5136.

Hauver K. and Ruzicka, A., 2011, Cohenite in NWA 5964 (L3-6 melt breccia): A possible product of shock-induced contact metamorphism: Houston, Texas, Lunar and Planetary Science Conference 42nd, abstract #2627.

Hutson, M., Ruzicka, A., Timothy Jull, A.J., Smaller, J.E., Brown, R., 2013, Stones from the Mohave County, Arizona: Multiple fall in the "Franconia strewn field": Meteoritics & Planetary Science, vol 48, Nr. 3, p. 365-389.

Hutson, M, Ruzicka, A., Pugh, R., Sloan, L., and Thompson, E., 2007, Complex brecciation and shock effects in the Buck Mountain Wash (H3-5) chondrite: Meteoritics & Planetary Science 42, N. 6, p. 963-978.

Hutson, M.L., Ruzicka, A.M., Farley, K.R., Schepker, K.L., Hugo, R.C., Likkel, L.E., 2016, Carbides in ordinary chondrites revisited, 47th Lunar and Planetary Science Conference, abstract #1377.

Huss, G.R., Rubin, A.E., and Grossman, J.N., 2006, Thermal Metamorphism in Chondrites: Meteorites and the early solar system II, University of Arizona Press: Tuscon p. 567-586.

Hutchison, R., 2004, Meteorites: a petrologic, chemical and isotopic synthesis: University Press, Cambridge, 506 p.

Jarosewich, E., 1990, Chemical analyses of meteorites: A compilation of stony and iron meteorite analyses: Meteoritics, vol. 25, p. 323-337.

Keller, L.P., 1998, A transmission electron microscope study of iron-nickel carbides in the matrix of the Semarkona unequilibrated ordinary chondrite: Meteoritics & Planetary Science, vol. 33(4), p. 913-919.

Krot, A. N., Keil, K., Goodrich, C. A., Scott, E. R. D., and Weisberg, M. K., 2005, Classification of meteorites, in Davis, A. M., Holland, H. D., and Turekian, K. K., eds., Meteorites, Comets and Planets: Treatise on Geochemistry, Volume 1: Elsevier BV, Amsterdam, Netherlands, p. 83-128.

Krot, A. N., Zolensky, M. E., Wasson, J. T., Scott, E. R., Keil, K., and Ohsumi, K., 1997, Carbide-magnetite assemblages in type-3 ordinary chondrites: Geochimica et Cosmochimica Acta, v. 61(1), p. 219-237.

Likkel L., Ruzicka, A. M., Hutson, M., Schepker, K., and Yeager T.R., 2013, Cohenite in chondrites: Further support for a shock-heating origin: Meteorit. Planet. Sci., Abstract #5145.

Okamoto, H., 1992. The C-Fe (carbon-iron) system. *Journal of Phase Equilibria*, *13*(5), pp.543-565, https://www.tf.uni-kiel.de/matwis/amat/iss/kap_6/illustr/s6_1_2.html.

Personal Communication with Secana Goudy.

Reisener, R.J., and Goldstein, J.I., 2003a, Ordinary chondrite metallography: Part 1. Fe-Ni taenite cooling experiments: Meteoritics & Planetary Science 38, Nr 11, p. 1669-1678.

Reisener, R.J., and Goldstein, J.I., 2003b, Ordinary chondrite metallography: Part 2. Formation of zoned and unzoned metal particles in relatively unshocked H, L, and LL chondrites: Meteoritics & Planetary Science 38, Nr 11, p. 1679-1696.

Romig Jr., A.D. and Goldstein, J.I., 1978, Determination of the Fe-rich portion of the Fe-Ni-C phase diagram: Metallurgical Transactions A, vol. 9A, p. 1599-1609.

Ruzicka, A.M., Hutson, M., Friedrich, J.M., Bland, P.A., Pugh, R., 2015, Northwest Africa 8709: A rare but revealing type 3 ordinary chondrite melt breccia: 78th Annual Meeting of the Meteoritical Society, Abstract #5348.

Schepker, K. L., 2014, Complex Thermal Histories of L Melt Breccias NWA 5964 and NWA 6580, [M.S. thesis]: Portland State University, 107 p.

Scott, E.R.D., and Goldstein, J.I., 2012, Occurrence of carbides and graphite in iron meteorites and origin of C-rich irons: 43rd Lunar and Planetary Science Conference, Abstract #2671.

Scott, E.R.D., and Rajan, R.S., 1981, Metallic minerals, thermal histories and parent bodies of some xenolithic, ordinary chondrite meteorites: Geochimica et Cosmochimica Acta, vol. 45, p. 53-67.

Scott, E.R.D., Krot, T.V., Goldstein, J.I., and Wakita, S., 2014, Thermal and impact history of the H chondrite parent asteroid during metamorphism: Constraints from metallic Fe-Ni: Geochimica et Cosmochimica Acta, v. 136, p. 13-37.

Scott E. R. D., Taylor G. J., and Maggiore P., 1982, A new LL3 chondrite, Allan Hills A79003, and observations on matrices in ordinary chondrites: Meteoritics v. 17, p. 65-75.

Stöffler, D., Bischoff, A., Buchwald, V., and Rubin, A. E., 1988, Shock effects in meteorites: Meteorites and the early solar system I, p. 165-202.

Stöffler, D., and Keil, K., 1991, Shock metamorphism of ordinary chondrites: Geochimica et Cosmochimica Acta, vol. 55, n. 12, p. 3845-3867.

Scorzelli, R.B., 2008, Meteorites: messengers from the outer space: Journal of the Brazilian Chemical Society, vol. 19, n. 2, p. 226-231.

Taylor, G.J., Maggiore, P., Scott, E.R.D, Rubin, A.E., and Keil, K., 1987, Original Structures, and Fragmentation and Reassembly Histories of Asteroids: Evidence from Meteorites: Icarus, vol. 69, p. 1-13.

Taylor G. J., Okada A., Scott E. R. D., Rubin A. E., Huss G. R., and Keil K., 1981, The occurrence and implications of carbide magnetite assemblages in unequilibrated ordinary chondrites: Lunar Planet. Sci. 12, 1076-1078 (abstr.)

Tomkins, A.G, 2009, What metal-troilite textures can tell us about post-impact metamorphism in chondrite meteorites: Meteoritics & Planetary Science 44, Nr 8, p. 1133-1149.

Tomkins, A.G., Mare, E.R., and Raveggi, M., 2013, Fe-carbide and Fe-sulfide liquid immiscibility in IAB meteorite, Campo del Cielo: Implications for iron meteorite chemistry and planetesimal core compositions: Geochimica et Cosmochimica Acta, vol. 117, p. 80-98.

Weisberg M. K., McCoy, T. J., and Krot, A. N., 2006, Systematics and evaluation of meteorite classification, in Lauretta, D. S. and McSween Jr., H. Y., eds., Meteorites and the Early Solar System II: University of Arizona Press, Tucson, p. 19-52.

Willis, J., and Goldstein, J.I., 1981, A revision of metallographic cooling rate curves for chondrites: Proc. Lunar Planet. Sci, v. 12B, p. 1135-1143.

Wood, J.A., 1967, Chondrites: their Metallic Minerals, thermal Histories, and Parent Planets: Icarus, v. 6, p. 1-49.